

# Recommendations and guidelines from the ISMIRM Diffusion Study Group for preclinical diffusion MRI: Part 1 — In vivo small-animal imaging

Ileana O Jelescu<sup>1,2,#</sup>, Francesco Grussu<sup>3,4</sup>, Andrada Ianus<sup>5</sup>, Brian Hansen<sup>6</sup>, Rachel L C Barrett<sup>7,8</sup>, Manisha Aggarwal<sup>9</sup>, Stijn Michielse<sup>10</sup>, Fatima Nasrallah<sup>11</sup>, Warda Syeda<sup>12</sup>, Nian Wang<sup>13,14</sup>, Jelle Veraart<sup>15</sup>, Alard Roebroeck<sup>16</sup>, Andrew F Bagdasarian<sup>17,18</sup>, Cornelius Eichner<sup>19</sup>, Farshid Sepehrband<sup>20</sup>, Jan Zimmermann<sup>21</sup>, Lucas Soustelle<sup>22</sup>, Christien Bowman<sup>23,24</sup>, Benjamin C Tandler<sup>25</sup>, Andreea Hertanu<sup>1</sup>, Ben Jeurissen<sup>26,27</sup>, Marleen Verhoye<sup>23,24</sup>, Lucio Frydman<sup>28</sup>, Yohan van de Looij<sup>29</sup>, David Hike<sup>17,18</sup>, Jeff F Dunn<sup>30,31,32</sup>, Karla Miller<sup>33</sup>, Bennett A Landman<sup>34</sup>, Noam Shemesh<sup>5</sup>, Adam Anderson<sup>36,35</sup>, Emilie McKinnon<sup>37</sup>, Shawna Farquharson<sup>38</sup>, Flavio Dell'Acqua<sup>39</sup>, Carlo Pierpaoli<sup>40</sup>, Ivana Drobnyak<sup>41</sup>, Alexander Leemans<sup>42</sup>, Kevin D Harkins<sup>43,35,44</sup>, Maxime Descoteaux<sup>45,46</sup>, Duan Xu<sup>47</sup>, Hao Huang<sup>48,49</sup>, Mathieu D Santin<sup>50,51</sup>, Samuel C. Grant<sup>17,18</sup>, Andre Obenaus<sup>52,53</sup>, Gene S Kim<sup>54</sup>, Dan Wu<sup>55</sup>, Denis Le Bihan<sup>56,57</sup>, Stephen J Blackband<sup>58,59,60</sup>, Luisa Ciobanu<sup>61</sup>, Els Fieremans<sup>62</sup>, Ruiliang Bai<sup>63,64</sup>, Trygve B Leergaard<sup>65</sup>, Jiangyang Zhang<sup>66</sup>, Tim B Dyrby<sup>67,68</sup>, G Allan Johnson<sup>69,70</sup>, Julien Cohen-Adad<sup>71,72,73</sup>, Matthew D Budde<sup>74,75</sup>, Kurt G Schilling<sup>43,35,#</sup>

#Corresponding authors — [ileana.jelescu@chuv.ch](mailto:ileana.jelescu@chuv.ch), [kurt.g.schilling.1@vumc.org](mailto:kurt.g.schilling.1@vumc.org)

<sup>1</sup>Department of Radiology, Lausanne University Hospital and University of Lausanne, Lausanne, Switzerland, <sup>2</sup>CIBM Center for Biomedical Imaging, Ecole Polytechnique Fédérale de Lausanne, Lausanne, Switzerland, <sup>3</sup>Radiomics Group, Vall d'Hebron Institute of Oncology, Vall d'Hebron Barcelona Hospital Campus, Barcelona, Spain, <sup>4</sup>Queen Square MS Centre, Queen Square Institute of Neurology, Faculty of Brain Sciences, University College London, London, UK, <sup>5</sup>Champalimaud Research, Champalimaud Foundation, Lisbon, Portugal, <sup>6</sup>Center of Functionally Integrative Neuroscience, Aarhus University, Aarhus, Denmark, <sup>7</sup>Department of Neuroimaging, Institute of Psychiatry, Psychology and Neuroscience, King's College London, London, UK, <sup>8</sup>NatBrainLab, Department of Forensics and Neurodevelopmental Sciences, Institute of Psychiatry, Psychology and Neuroscience, King's College London, London, UK, <sup>9</sup>Russell H. Morgan Department of Radiology and Radiological Science, Johns Hopkins University School of Medicine, Baltimore, MD, USA, <sup>10</sup>Department of Neurosurgery, School for Mental Health and Neuroscience (MHeNS), Maastricht University Medical Center, Maastricht, The Netherlands, <sup>11</sup>The Queensland Brain Institute, The University of Queensland, Queensland, Australia, <sup>12</sup>Melbourne Neuropsychiatry Centre, The University of Melbourne, Parkville, Victoria, Australia, <sup>13</sup>Department of Radiology and Imaging Sciences, Indiana University, IN, USA, <sup>14</sup>Stark Neurosciences Research Institute, Indiana University School of Medicine, IN, USA, <sup>15</sup>Center for Biomedical Imaging, NYU Grossman School of Medicine, New York, NY, USA, <sup>16</sup>Faculty of psychology and Neuroscience, Maastricht University, Maastricht, Netherlands, <sup>17</sup>Department of Chemical & Biomedical Engineering, FAMU-FSU College of Engineering, Florida State University, Tallahassee, FL, USA, <sup>18</sup>Center for Interdisciplinary Magnetic Resonance, National High Magnetic Field Laboratory, Tallahassee, FL, USA, <sup>19</sup>Department of Neuropsychology, Max Planck Institute for Human Cognitive and Brain Sciences, Leipzig, Germany, <sup>20</sup>USC Stevens Neuroimaging and Informatics Institute, Keck School of Medicine of USC, University of Southern California, Los Angeles, CA, USA, <sup>21</sup>Department of Neuroscience, Center for Magnetic Resonance Research, University of Minnesota, MN, USA, <sup>22</sup>Aix Marseille Univ, CNRS, CRMBM, Marseille, France, <sup>23</sup>Bio-Imaging Lab, Faculty of Pharmaceutical, Biomedical and Veterinary Sciences, University of Antwerp, Antwerp, Belgium, <sup>24</sup>μNEURO Research Centre of Excellence, University of Antwerp,

Antwerp, Belgium, <sup>25</sup>Wellcome Centre for Integrative Neuroimaging, FMRIB, Nuffield Department of Clinical Neurosciences, University of Oxford, United Kingdom, <sup>26</sup>imec Vision Lab, Dept. of Physics, University of Antwerp, Belgium, <sup>27</sup>Lab for Equilibrium Investigations and Aerospace, Dept. of Physics, University of Antwerp, Belgium, <sup>28</sup>Department of Chemical and Biological Physics, Weizmann Institute of Science, Rehovot, Israel, <sup>29</sup>Division of Child Development & Growth, Department of Pediatrics, Gynaecology & Obstetrics, School of Medicine, Université de Genève, Genève, Switzerland, <sup>30</sup>Department of Radiology, Cumming School of Medicine, University of Calgary, Calgary, Alberta, Canada, <sup>31</sup>Hotchkiss Brain Institute, Cumming School of Medicine, University of Calgary, Calgary, Alberta, Canada, <sup>32</sup>Alberta Children's Hospital Research Institute, Cumming School of Medicine, University of Calgary, Calgary, Alberta, Canada, <sup>33</sup>FMRIB Centre, Wellcome Centre for Integrative Neuroimaging, Nuffield Department of Clinical Neurosciences, University of Oxford, Oxford, United Kingdom, <sup>34</sup>Department of Electrical and Computer Engineering, Vanderbilt University,, <sup>35</sup>Vanderbilt University Institute of Imaging Science, Vanderbilt University, Nashville, TN, <sup>36</sup>Department of Radiology and Radiological Sciences, Vanderbilt University Medical Center, Nashville, TN, USA, <sup>37</sup>Medical University of South Carolina, Charleston, SC, USA, <sup>38</sup>National Imaging Facility, The University of Queensland, Brisbane, Australia, <sup>39</sup>Department of Forensic and Neurodevelopmental Sciences, King's College London, London, UK, <sup>40</sup>Laboratory on Quantitative Medical imaging, NIBIB, National Institutes of Health, Bethesda, MD, USA, <sup>41</sup>Department of Computer Science, University College London, London, UK, <sup>42</sup>PROVIDI Lab, Image Sciences Institute, University Medical Center Utrecht, The Netherlands, <sup>43</sup>Radiology and Radiological Sciences, Vanderbilt University Medical Center, Nashville, TN, USA, <sup>44</sup>Biomedical Engineering, Vanderbilt University, Nashville, TN, <sup>45</sup>Sherbrooke Connectivity Imaging Lab (SCIL), Computer Science department, Université de Sherbrooke, <sup>46</sup>Imeka Solutions, <sup>47</sup>Department of Radiology and Biomedical Imaging, University of California San Francisco, CA, USA, <sup>48</sup>Department of Radiology, Perelman School of Medicine, University of Pennsylvania, Philadelphia, PA, USA, <sup>49</sup>Department of Radiology, Children's Hospital of Philadelphia, Philadelphia, PA, USA, <sup>50</sup>Centre for Neuroimaging Research (CENIR), Inserm U 1127, CNRS UMR 7225, Sorbonne Université, Paris, France, <sup>51</sup>Paris Brain Institute, Paris, France, <sup>52</sup>Department of Pediatrics, University of California Irvine, Irvine CA USA, <sup>53</sup>Preclinical and Translational Imaging Center, University of California Irvine, Irvine CA USA, <sup>54</sup>Department of Radiology, Weill Cornell Medical College, New York, NY, USA, <sup>55</sup>Key Laboratory for Biomedical Engineering of Ministry of Education, College of Biomedical Engineering & Instrument Science, Zhejiang University, Hangzhou, China, <sup>56</sup>CEA, DRF, JOLIOT, NeuroSpin, Gif-sur-Yvette, France, <sup>57</sup>Université Paris-Saclay, Gif-sur-Yvette, France, <sup>58</sup>Department of Neuroscience, University of Florida, Gainesville, FL, United States, <sup>59</sup>McKnight Brain Institute, University of Florida, Gainesville, FL, United States, <sup>60</sup>National High Magnetic Field Laboratory, Tallahassee, FL, United States, <sup>61</sup>NeuroSpin, UMR CEA/CNRS 9027, Paris-Saclay University, Gif-sur-Yvette, France, <sup>62</sup>Department of Radiology, New York University Grossman School of Medicine, New York, NY, USA, <sup>63</sup>Interdisciplinary Institute of Neuroscience and Technology, School of Medicine, Zhejiang University, Hangzhou, China, <sup>64</sup>Frontier Center of Brain Science and Brain-machine Integration, Zhejiang University, <sup>65</sup>Department of Molecular Biology, Institute of Basic Medical Sciences, University of Oslo, Norway, <sup>66</sup>Department of Radiology, New York University School of Medicine, NY, NY, USA, <sup>67</sup>Danish Research Centre for Magnetic Resonance, Centre for Functional and Diagnostic Imaging and Research, Copenhagen University Hospital Amager & Hvidovre, Hvidovre, Denmark, <sup>68</sup>Department of Applied Mathematics and Computer Science, Technical University of Denmark, Kongens Lyngby, Denmark, <sup>69</sup>Duke Center for In Vivo Microscopy, Department of Radiology, Duke University, Durham, North Carolina, <sup>70</sup>Department of Biomedical Engineering, Duke University, Durham, North Carolina, <sup>71</sup>NeuroPoly Lab, Institute of Biomedical Engineering, Polytechnique Montreal, Montreal, QC, Canada, <sup>72</sup>Functional Neuroimaging Unit, CRIUGM, University of Montreal, Montreal, QC, Canada, <sup>73</sup>Mila - Quebec AI Institute, Montreal, QC, Canada, <sup>74</sup>Department of Neurosurgery, Medical College of Wisconsin, Milwaukee, Wisconsin, <sup>75</sup>Clement J Zablocki VA Medical Center, Milwaukee, Wisconsin

## Abstract

The value of *in vivo* preclinical diffusion MRI (dMRI) is substantial. Small-animal dMRI has been used for methodological development and validation, characterizing the biological basis of diffusion phenomena, and comparative anatomy. Many of the influential works in this field were first performed in small animals or *ex vivo* samples. The steps from animal setup and monitoring, to acquisition, analysis, and interpretation are complex, with many decisions that may ultimately affect what questions can be answered using the data. This work aims to serve as a reference, presenting selected recommendations and guidelines from the diffusion community, on best practices for preclinical dMRI of *in vivo* animals. In each section, we also highlight areas for which no guidelines exist (and why), and where future work should focus. We first describe the value that small animal imaging adds to the field of dMRI, followed by general considerations and foundational knowledge that must be considered when designing experiments. We briefly describe differences in animal species and disease models and discuss how they are appropriate for different studies. We then give guidelines for *in vivo* acquisition protocols, including decisions on hardware, animal preparation, imaging sequences and data processing, including pre-processing, model-fitting, and tractography. Finally, we provide an online resource which lists publicly available preclinical dMRI datasets and software packages, to promote responsible and reproducible research. An overarching goal herein is to enhance the rigor and reproducibility of small animal dMRI acquisitions and analyses, and thereby advance biomedical knowledge.

**Keywords:** preclinical; diffusion MRI; small animal; best practices; microstructure; diffusion tensor; tractography; acquisition; processing; open science.

<b>1 Introduction</b>	5
<b>2 Added Value</b>	7
2.1 Small-animal diffusion MRI: Added value	7
2.2 Translation and validation considerations	10
2.3 Species differences	14
2.3.1 Murine models (mouse and rat)	15
2.3.2 Primate models	16
2.3.3 Other models	17
<b>3 Acquisition</b>	17
3.1 Standard Protocol - overview	17
3.2 Hardware (species/organ specific)	20
3.2.1 RF Coils	20
3.2.2 Gradients	21
3.2.3 Magnet & field strength	22
3.2.4 Where future work should lie	22
3.3 Animal preparation & physiological monitoring	23
3.4 Acquisition: diffusion encoding	24
3.5 Acquisition: signal readout	27
3.6 Acquisition: q-t coverage	28
3.7 Acquisition: Spatial resolution	33
<i>Volume equivalent resolutions and pushing the boundaries</i>	34
<b>4 Data Processing</b>	35
4.1 Pre-processing pipeline	35
4.1.1 Brain	36
4.1.2 Cord & other organs	40
4.1.3 Where future work should lie	41
4.2 Processing pipelines	42
4.2.1 Where future work should lie	42
4.3 Tractography	43
4.3.1 Where future work should lie	45
<b>5 Perspectives</b>	46
5.1 Open science	46
5.1.1 Code/Software	46
5.1.2 Data Sharing & Databases	47
5.1.3 Where future work should lie	48
5.2 The future: what should we strive to achieve?	49
<b>6 Acknowledgements and Support</b>	51
<b>7 References</b>	53

# 1 Introduction

Diffusion magnetic resonance imaging (dMRI) is a medical imaging technique that utilizes the diffusion of water molecules to generate image contrast, enabling the non-invasive mapping of the diffusion process in biological tissues. Because molecular diffusion in tissue is hindered or restricted by interactions with tissue components including membranes and macromolecules, the diffusion patterns can reveal microscopic details of tissue architecture in both normal and abnormal states. Thus, dMRI can be used to generate a wide range of maps which highlight different properties of the tissue microstructure. Additionally, dMRI is widely applied to map the orientations of white matter fibers to study the structural connections of the brain in a process called fiber tractography. These microstructure and connectivity maps have often been described as a non-invasive 'virtual histology' or 'virtual dissection' and have found applications widely used in neuroanatomy, developmental, cognitive, and systems neuroscience, neurology, and neuroevolution for exploring neural architecture in healthy and disease afflicted brains.

Both *in vivo* dMRI studies of small animals and of *ex vivo* specimens derived from animal or human tissues, have greatly benefited and increased scientific knowledge in the field of diffusion MRI, much like any biomedical or behavioral research field. In this work, **we define small animal imaging as imaging performed on a living animal model of human tissue, whereas *ex vivo* we define as covering perfused living tissue or fixed tissue - the latter is covered in a separate paper, 'Part 2'**. Small-animal dMRI has been used for methodological development and validation, characterizing the biological basis of diffusion phenomena, and comparative anatomy. Many of the influential works in this field were first performed in small animals or *ex vivo* samples. For example, the discovery of a dramatic decreased diffusivity in cerebral ischemia was first observed in a cat model (1), diffusion tensor imaging formalism was originally validated on vegetable, pork loin, and rabbit models (2,3), and diffusion anisotropy was first observed again in cat models (4) (and reproduced postmortem to prove anisotropy was not due to motion). Microstructural and tractography models of today are routinely validated against animal models, *ex vivo* scans, and subsequent histological analysis (4–7).

The science of dMRI covers many disciplines and is continually evolving. The steps from animal setup and monitoring, to acquisition, analysis, and interpretation are complex, with many decisions that may ultimately affect what questions can be answered using the data. To elucidate some salient factors influencing acquisitions and interpretations of dMRI, this work aims to serve as a reference, presenting selected recommendations and guidelines from the diffusion community, on best practices for preclinical dMRI of *in vivo* animals.

**This work does not serve as a “consensus” on any specific topic, but rather as a snapshot of “best practices” or “guidelines”** from the preclinical dMRI community as represented by the authors. Recruitment for participation in this effort included two meetings of the Diffusion Study Group of the International Society for Magnetic Resonance in Medicine, responses to a survey distributed within the Diffusion Study Group forum, and recommendations for recruitment from other authors. We envision this work to be useful to imaging centers using small animal scanners for research, sites that may not have personnel with expert knowledge in diffusion, pharmaceutical or industry employees who may want to run their own tests and studies, or new trainees in the field of dMRI. The resources provided herein may act as a starting point when reading the literature, and understanding the decisions and processes for studying model systems with dMRI.

The manuscript is organized as follows. We first describe the **value** that small animal imaging adds to the field of dMRI, followed by **general considerations and foundational knowledge that must be considered when designing experiments**. We briefly describe **differences in species and models** and discuss why some may be more or less appropriate for different studies. We then give guidelines for ***in vivo* acquisition protocols**, including decisions on hardware, animal preparation, and imaging sequences, followed by guidelines for **data processing** including pre-processing, model-fitting, and tractography. Finally, we give **perspectives** on the field, describing **sharing of code and data**, and **goals** that we wish to achieve. In each section, we attempt to provide guidelines and recommendations, but also highlight areas for which no guidelines exist (and why), and where future work should lie. An overarching goal herein is to **enhance the rigor and reproducibility** of small animal dMRI acquisitions and analyses, and thereby advance biomedical knowledge.

## 2 Added Value

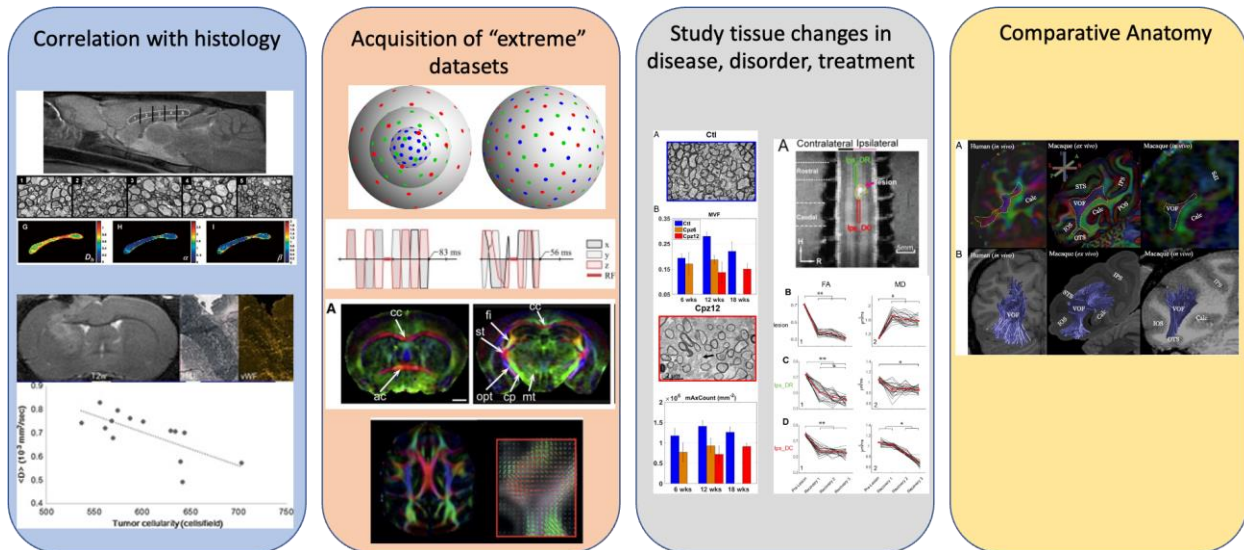


**Figure 1.** Four areas in which preclinical brain imaging adds value to the field of dMRI. It enables: (i) correlation with histology on the same subject/sample, (ii) the acquisition of richer datasets than on clinical systems thanks to more advanced hardware and longer scan times available, (iii) the study of tissue changes with disease and treatment in a more controlled setting, and (iv) comparative anatomy between species. Figures reused and adapted from (i) (8,9) (ii) (10–13) (iii) (14,15) (iv) (16)

### 2.1 Small-animal diffusion MRI: Added value

Small animal models add substantial value to dMRI, acting as supplements, substitutes, and/or validation mechanisms for *in vivo* human studies. While important differences exist in not only morphology and biology, but also MR acquisition and analysis, these model systems improve our understanding of dMRI contrast, and provide insight into anatomy and physiology over a range of spatial scales, from the microstructural properties of tissue to the macro-scale connectivity of fiber pathways in the brain. Here, we describe four areas in which small animal imaging brings added value to the field of dMRI (**Figure 1**).

**First, small animal dMRI allows correlations with histological and other (invasive) imaging measures** to discover the biophysical basis of the dMRI signal, parameters, and biomarkers that we are measuring. The holy grail of dMRI is to ultimately offer the ability to act as a non-invasive *in vivo* microscopic tool, and perform non-invasive diagnostic imaging with sensitivity and specificity almost approaching post mortem histological or histopathological microscopic measures, serving as a sort of “virtual *in vivo* histology” or “virtual *in vivo* dissection”

of tissue. As the imaging technology and strategies move closer to this goal, it becomes critical to validate novel techniques and biophysical models by directly comparing dMRI findings to histological measures, axonal tracers, and other detailed tissue preparations. A wide range of tools exist for conventional analysis of microstructure and connectivity, as well as more recent advances in tissue preparation and light microscopy, that allow 3D visualization of tissue organization with sub-cellular resolution and the possibility of selective staining of tissue components. The use of animal models allows both MRI scanning and subsequent quantitative histological analysis. Through co-registration of microscopy images to MRI images of the same specimens, direct comparisons and correlation of dMRI measures to different quantitative microscopic parameters can be achieved, thus elucidating how different microscopic tissue features influence dMRI contrast, and increase insight into how sub-voxel tissue architecture can be assessed using dMRI techniques. Such validation studies in turn improve our ability to interpret *in vivo* dMRI for both preclinical and clinical studies and open new avenues for diagnostic imaging, disease monitoring and treatment, as well as non-invasive mapping of brain structure and function.

**Second, small animal imaging allows acquisition of “extreme” datasets**, at the edge of what is achievable in dMRI in terms of spatial resolution and/or  $q$ - $t$  coverage, and clearly beyond what is currently achievable with clinical imaging. Thus, preclinical dMRI contributes to pushing the boundaries of acquisition and analysis to answer questions about what dMRI is capable of measuring in principle. A distinct advantage of preclinical imaging is the ability to use higher field strengths, with typically much stronger gradients, specie/sample-dedicated RF coils, and for longer scan times. Together these allow the acquisition of images with much higher signal to noise ratio (SNR), with more advanced diffusion encoding and stronger diffusion sensitization (i.e., higher  $b$ -values). **Magnetic field.** In practice, the SNR increases linearly or better than linearly with field strength (17), accounting for all competing effects. Thus high-field, small-bore magnets typical of animal imaging (with field strengths currently reaching as high as 21T), in combination with the use of **small well-tailored coils** (18), provide substantial advantages of having higher SNR, including the possibility of achieving higher image resolution. **Gradients.** Additionally, while clinical systems are typically equipped with 40 - 80 mT/m magnetic field gradients, those on small animal MRI systems are very often 300 mT/m or higher, with 1 T/m becoming more and more widespread. Dedicated inserts at 3 T/m (along all three axes) are also commercially available. Strong field gradients ( $G$ ) are an immense asset for dMRI experiments because they allow faster encoding and read-out and an independent or largely decorrelated exploration of the two dimensions of  $q$ - $t$  space — where  $q$  is the spatial phase warp that introduces diffusion sensitization

( $q = \gamma\delta G$ ) and  $t$  is the diffusion time imparted for the molecules to diffuse and explore the local environment, the combination of the two giving the “ $b$ -value” that quantifies overall diffusion weighting ( $b = q^2 t$ ). Indeed, while on clinical systems high  $b$ -values are typically only achieved by increasing the diffusion time and/or the gradient pulse duration  $\delta$ , strong gradients give access to high  $q$ -values and thus  $b$ -values for a broad range of diffusion times  $t$ . Unique insights into diffusion signal behavior, and thus into the underlying microstructure, have been brought by exploring a range of  $q$ - $t$  space only possible (at the time) on animal systems, including very short diffusion times (19–22), very strong diffusion weightings (23,24) or more complex diffusion encoding schemes (25–27). **Scan time.** Finally, preclinical dMRI also offers the possibility for additional scan time, often more than human studies, but do have a limitation as typically stated in the ethical protocol. Extended scanning facilitates acquisitions across  $q$ - $t$  ranges with high resolution and substantially increased SNR. For these reasons, the combination of high magnetic field strengths, and fast high-amplitude gradients enables “extreme” acquisitions currently impossible on clinical scanners, pushing the scientific boundaries of what can be studied with these unique contrasts.(19–22)

**Third, the use of animal models allows us to study the sensitivity of dMRI to tissue changes in diseases, disorders and treatments in a controlled way** that is not always possible in the human, allowing the knowledge gain to be applied to human studies. Put simply, the use of small animal imaging has similar value to all other biomedical research, in that it allows experimental testing that would not be possible or practical in humans. Changes in diffusion contrast can be studied across a large range of animal models of disease and dysfunction, animal models may be better controlled than patient groups, and small animal MRI can be multimodal, easily longitudinal, and supported by behavior analysis and (as stated above) histology from the same animals. Prominent examples include longitudinal imaging after carefully controlled acute injuries (stroke, TBI, spinal cord injury), testing effects of drugs/treatment (28,29), or functional characterization of neuromodular targets. Thus, small animal systems allow ‘better’ imaging - faster, with higher spatial and displacement resolution - than is ever possible on clinical machines at a given technological time point: small animal dMRI data will always help interpret less resolved and more limited human dMRI data. As such, preclinical systems provide the stepping stones for development and validation of biomarkers, diagnosis, and monitoring changes over time or in response to treatment.

**Fourth, the use of animal models enables comparative anatomy**, allowing the investigation of key differences between human and other mammalian brains, to gain insights into the evolutionary changes that separate humans from animals. The differences in animal strains

and species provide an unequalled opportunity to mimic the polymorphic differences of human diseases which allows for a better understanding of the development of disease, its temporal evolution, and treatment options (30,31). Animal models have been fundamental in our understanding of the topographic ordering of cortical and subcortical connections; humans and animals share analogous features of structural and functional brain networks that support core cognitive properties closely related to behavior (32,33) making them a holistic platform for the investigation of comparative anatomy. A key challenge in comparative neuroanatomy is to identify homologous structures and structural boundaries across species. Moreover, the brain undergoes substantial changes through development and aging which hampers comparison of data from different timepoints. *In vivo* dMRI maps facilitate identification of corresponding tissue features across species and ages.

In summary, dMRI in small animals allows researchers to perform these studies non-invasively, with all the added values described above, over the whole brain (compared to previous histological or invasive studies limited to a few regions or pathways), and with the possibility to conduct longitudinal analysis.

## 2.2 Translation and validation considerations

While small animal models enable us to perform histological validation, acquisition of extreme datasets, sensitive studies of disease, and comparative anatomy, several aspects must be considered when designing and performing experiments to appropriately interpret scientific results. Below, we discuss considerations in the tissue model itself, disease and disorders, and hardware and experimental setup. While the diffusion process is fundamentally the same, and governed by the same laws of physics, these must be carefully thought out to translate findings to the *in vivo* human.

### **Anatomical considerations**

Basic constituents of the brain and other organs are largely preserved across mammalian species, providing a basis for translational *in vivo* MRI studies. In the **central nervous system**, the fundamental structure of a long axon with a myelin sheath makes the signal interpretation in white matter fundamentally translatable, although nuances exist as to the axon diameter, myelin thickness and ratio of myelinated to unmyelinated axons (34,35). Brain cortical layers are also largely preserved across species. However, while the ratio of white-to-gray matter is <1 in most

species, including most primates, is very different between rodents and primates, with predominant gray matter, unfolded cortex and thin white matter tracts in rodents, and relatively more white matter and folded cortex in primates (see (36) for a comprehensive characterization of white-to-gray ratio and cortical folding patterns across mammalian species). As a result, the partial volume effects are more challenging to mitigate in rodent white matter and in human/primate gray matter, respectively. The complexity of the rodent white matter organization also does not match that of primate, resulting in potential issues when translating modeling and tractography approaches from the rodent brain. Like humans, some species have a gyrencephalic cortex, such as sheep, pigs and ferrets, while rodents do not. However, large bundles such as corpus callosum or the external capsule retain structure similarity, even in rodents.

For **other organs**, intrinsic differences in microstructure do exist, such as much larger hepatocytes in mouse liver compared to humans (37,38), should be carefully accounted for. In addition to the differences in anatomy, the preclinical studies often offer limited biological diversity, as the animals typically share similar genetic and environmental background, which is in contrast to human studies with inherently diverse demographic characteristics. Genetic diversity can be enhanced, particularly in mice, by the use of congenic mouse lines (39).

### **Considerations in disease/disorder/model**

It remains difficult to confirm the translational value of animal models of genetic disorders or psychiatric diseases due to the uncertainty of disease mechanism(s) and the difficulty of replicating the mechanism in animals. However, brain injury models, such as traumatic brain injury (TBI), epilepsy, stroke, subarachnoid and intracerebral hemorrhage, spinal cord injury, edema or de/re-myelination have high translational value since the cellular responses to the external insults are similar between species (40,41). Tumor models may also display some translational value. A remarkable animal model to study the fundamental properties of naturally occurring neuroplasticity are songbirds. In particular, open-ended learners like starlings are relevant since they experience seasonal changes in song behavior, which are related to structural changes within their song control system. Zebra finches are closed-ended learners, which represent a valid model to study particular aspects of vocal learning and communication, displaying convincing parallels with e.g. human speech. Even if animal models are not directly translatable, they may offer partial systemic deficits that mimic relevant aspects of the disease (i.e. altered microstructure or connectivity).

Animal **injury models** are widely used for monitoring the injury processes and assessment of treatment strategies. For instance, dMRI is conveniently used to longitudinally

monitor the disease progression in rodent models of hypoxic-ischemic encephalopathy (HIE), in which the apparent diffusion coefficient (ADC) first drops and then rebounds during reperfusion (42,43). Studies of altered myelination have been instrumental in characterizing the sensitivity and specificity of diffusion and kurtosis tensor metrics, as well as parameters of biophysical models of diffusion in white matter as potential biomarkers of these mechanisms, applicable *in vivo* to multiple sclerosis and other demyelinating diseases. Common models include cuprizone-induced demyelination and spontaneous remyelination, experimental autoimmune encephalomyelitis or transgenic mouse models of hypomyelination (14,44–48). In traumatic brain injury (TBI), evidence from animal studies has been pivotal in our understanding of the phasic changes in DTI measures; FA increases in the acute phase have been associated with neural plasticity and axonal regrowth (49–51), while chronic decreases in FA were related to elevated markers of diffuse axonal injury on histology and electron microscopy (52,53). These findings are consistent with human studies of TBI where an increase and decrease in FA has been reported in the acute and chronic phases post-injury, respectively (54,55). The above examples provide clear evidence on the informed translational knowledge that animal studies provide to our understanding of DTI metrics. Preclinical imaging studies of animal models are important because in combination with histology they offer insight into diseases where there is a mismatch between radiologically visible brain abnormality and clinical disability (the so-called clinico-radiological paradox). With appropriate animal models we have the opportunity to develop imaging techniques with sufficient sensitivity to reconcile radiological marker scores with observed severity of symptoms and overall disease burden.

Small animal **tumor models** have been extensively used to investigate the potential of dMRI in cancer research. Several studies showed that diffusivity is sensitive to early changes in tumor induced by chemoradiation therapy (56–58). Other dMRI metrics, such as intravoxel incoherent motion (IVIM) and diffusion kurtosis, have also been compared with tumor biological and physiological aspects using animal tumor models (9,59,60). However, it is not straightforward to extrapolate these findings from animal models to patients, partly due to substantial differences in tumor characteristics and host environment between these models and human cancers (61). But more importantly for dMRI, there is often a major difference in terms of achievable diffusion times between small animal studies and clinical studies (10 ms vs >50 ms, respectively). However, diffusion metrics measured at such different diffusion times will not be sensitive to the same aspects and spatial scales of the micro-environment. Previous studies demonstrated that diffusivity measurements below 100 ms vary substantially depending on tumor cell size and extracellular volume fraction (62–66), unlike in the healthy brain tissue where cellular size is much

smaller than in tumors (on the order of 1  $\mu\text{m}$ ) and packing density is higher. Hence, in addition to careful selection of appropriate animal models relevant to the corresponding clinical situation, the diffusion time should be considered carefully when conducting a dMRI study of small animal tumor models for validation of clinical study results. This will maximize the chance for the outcome to translate to clinical applications.

Another important advantage of animal vs human *in vivo* imaging is the opportunity for **longitudinal studies** where a larger portion of the lifespan can be probed in less time than in human studies. This may greatly facilitate studies of development, for example studying development from birth to young adult age in a matter of weeks for the rat, and many more small animals (67). While there are indeed a number of ongoing longitudinal human studies, variables and confounds across the longitudinal study are much easier to control in animal cohorts than humans. Processes such as brain development, aging and plasticity have been extensively characterized using *in vivo* longitudinal dMRI in a variety of species, from rodents (68–74) to non-human primates (75–78). The evolution of disease in animal models has also brought significant insight into pathological mechanisms for Alzheimer's (79–81), Huntington's (82), development pathologies (83), and many more (84). Other models include phenotyping of risk genes of neuropsychiatric disorders (85). The main limitation to the translation of these findings is similar to that mentioned previously: potential differences in physiological and pathological processes between animal models and humans. For example, developmental processes and epochs differ substantially between humans and animals and often insufficient effort is placed in selection of the appropriate time points (86).

### **Considerations in hardware and acquisition strategies**

*In vivo* acquisitions in small animals can be run with fewer constraints for scan time, for deposited RF power (specific absorption rate - SAR), or peripheral nerve stimulation from rapid gradient switching. Preclinical acquisition parameters in terms of  $q$ - $t$  coverage are typically also out of reach in the clinic. This is a significant advantage to animal imaging, enabling the exploration of signal contrast that would otherwise be too noisy with clinical hardware, but that can be subsequently optimized or fine-tuned for clinical experiments.

At the same time, the added value of pre-clinical imaging in terms of exploring territory unattainable on clinical scanners may also limit the translatability. As an example, the diffusion times used in small animal dMRI are typically minimized to around 10 ms to reduce TE and have optimal SNR. On clinical scanners, on the other hand, employed diffusion times are longer, typically around 50 ms and up. These discrepancies in diffusion times may result in a diffusion

contrast driven by different microstructural features, and/or in different regimes of diffusion time-dependence.

Finally, the effect of animal anesthesia may also be considered, although this is much more of a confounding factor in functional MRI studies, and there is increasing interest for awake animal experiments with MRI alone and in combination with optical techniques (87).

## 2.3 Species differences

Diffusion MRI has become the go-to tool when studying the brain anatomy due to its noninvasive and quantitative nature and intricate delineation of deep brain structures. It has been applied in a number of species including birds (88), mice (89–92), rats (93–95), canines (96), ferrets (53), pigs ((97)), monkeys, (98–102), great apes (103–106), sheep (107,108), and humans (109).

The most appropriate species to investigate is ultimately dependent upon the research question, as some species are more appropriate than others for a given study - for example one species may facilitate replication of neurological conditions, whereas another may better reflect the biology or structural connectivity of the human brain. In general, among several possible species that are appropriate models, the one with the least experimental hurdles and the minimum cost will be chosen. **Figure 2** shows images from several species, ranging from the smaller rodent and bird-brains to the non-human primates and humans. Images are colored based on estimates of WM (blue), gray matter (green), and CSF (red, if applicable). Differences in size, structure, complexity, and tissue volumes are immediately apparent.

Clearly, different model systems have their own advantages and disadvantages. Below, we list some of the most common (and less common) species studied with dMRI and briefly describe advantages and disadvantages of each. We underline that ethical and cost issues are important factors to consider when working with any species, or choosing between species. Here we focus mainly on the scientific aspects.

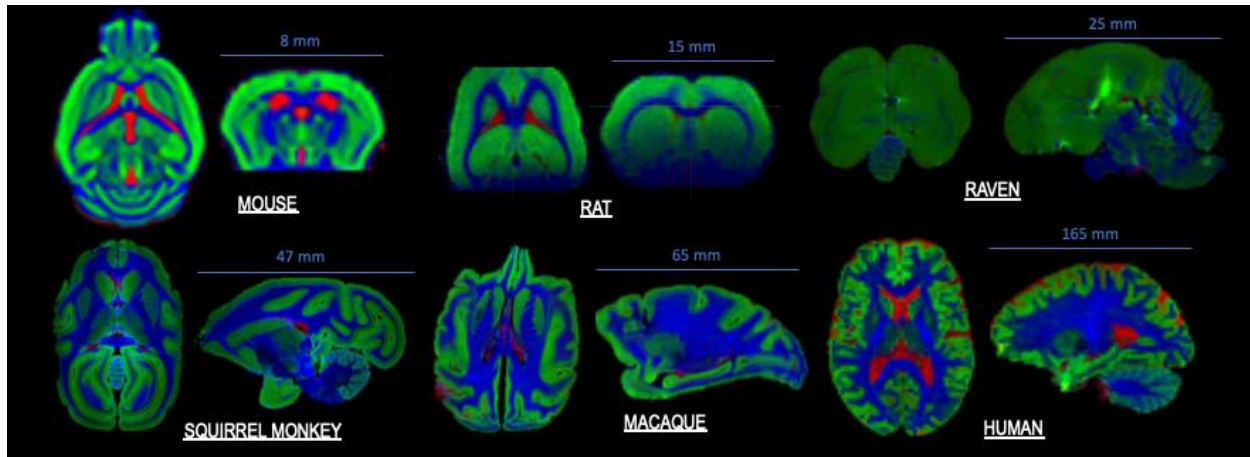


**Figure 2.** dMRI brain images of different small animal models demonstrating different brain sizes, geometric complexity, gyrification, and tissue constituents, ordered by increasing complexity. Different tissue types are estimated using Multi-Shell Multi-Tissue Spherical Deconvolution (110) and color coded - CSF (red), GM (Green), and WM (blue). *In vivo* data: mouse, rat, human. *Ex vivo* data: raven, squirrel monkey, macaque. Data kindly provided by Adam Anderson, Ileana Jelescu, Kurt Schilling, Ben Jeurissen and Marleen Verhoye.

### 2.3.1 Murine models (mouse and rat)

Rats and mice have been and continue to be the long-standing preferred species for biomedical research models as they offer a low-cost option with outcome measures widely available and a substantial database of normative data, including behavioral, genomic, and medical imaging. For this reason, the murine models have become popular small-animal models in dMRI.

Other advantages include wide availability, group homogeneity, well-characterized transgenic models simulating human pathology, and the very rapid lifespan, much shorter than that of larger animal species. The ability, at least in mice, to rapidly insert human genes allows great flexibility pursuing genomic functional changes that may mimic the human condition (note: the investigator bears the responsibility of confirming appropriate insertion into the recipient genome and verifying if genetic drift has occurred). In addition to biological advantages, the small physical size offers technical advantages, fitting in the typically smaller bores (and smaller coils) of magnets with larger field strengths.

While the advantages of the murine models are numerous, it is important to note the multiple anatomical differences from human structures, highlighted in [Section 2.2 Anatomical considerations](#), including smaller size, less gyrification, and less white matter. Such anatomical differences have also been associated with underlying molecular correlates (111), and most importantly limit the direct translatability of dMRI findings from murine models to humans.

Finally, mouse models are common in studies focussing on dMRI development/validation outside the central nervous system, as for example in oncological application. For instance, BALB/c mice, NOD.Cg-Prkdc<sup>scid</sup> IL2rg<sup>tm1Wjl</sup>/SzJ mice and Sprague-Dawley rats have been used in liver dMRI (112,113); C57BL/6 mice have been used to study dMRI in prostate and seminal vesicles (114); nude MF1 NU/NU mice in colorectal cancer xenograft models (115).

In summary, murine models are particularly suited for studies where models that replicate human neurological disease exist, for low-cost exploratory investigations on *in vivo* systems, particularly for probing the basis of non-Gaussian diffusion or even body IVIM experiments, for histological validation of acquisitions and models, and for investigations of single fiber population structures like the corpus callosum. Because of the larger ratio of gray-to-white matter, murine models may also be well-suited for studies of gray matter anatomy and physiology.

### 2.3.2 Primate models

Non-human primates (NHPs) most-often offer a model of tissue microstructure and structural connectivity that is closer to the human than rodents. Popular NHPs in dMRI literature include marmosets, squirrel monkeys, and macaques. These species have been popular models in psychological, evolutionary, and biological sciences since before dMRI, and are most often used to validate structural connectivity measurements, although they have also been used as preclinical models of disease or injury.

The monkey is commonly used in neuroscience research because it has a large number of white matter and gray matter regions with homologous counterparts in humans. The use of NHP allows access to “ground truth” connectivity, which has been well-documented through the use of tracer and ablation studies (116). Because of this, several NHP brain atlases exist, both in printed and digital form (104,117–121), which allow localization and comparison across subjects and across time.

NHPs are very well suited for studies of specific pathways and their structural and functional significance. For example, controversies regarding the existence or nonexistence of a pathway, or the location of pathway terminations have been resolved or steered through primate models (102,122–124), and a number of tractography validation studies have used tracer studies in primates or used primates to identify limitations in these processes (125–128), although validation is most commonly performed on *ex vivo* samples prior to histological analysis (129–138).

The disadvantages of NHPs are most often associated with access costs. Complex housing is required, as well as training for transportation to the scanner and preparation for

scanning, which is often not available at all locations. Lastly, small bore preclinical systems and high performing gradient inserts are often not large enough for bigger brains and the accompanying radiofrequency hardware. Because of this, NHPs have a much reduced availability compared to rodent models. Finally, ethical issues are even more complex than for murine models. Because of the growing evidence of intelligence and complex social skills, it is critical to continually ensure responsible research on NHPs. As a result of such ethical concerns, invasive biomedical research (including anesthetized *in vivo* imaging) on great apes has been banned in many nations for several years. Therefore, further *in vivo* imaging of NHPs is only possible in evolutionarily more distant NHPs such as monkeys.

Primate species must also be considered for each experiment: smaller monkeys (galago, squirrel monkey) may be easier to work with, less cumbersome to scan, less expensive to house, and the reduced gyrification makes cortical identification easier (for example for injections or electrical stimulation).

Overall, NHPs are particularly well suited for studies of cortical development, gyrification, and interrogation of complex white matter. Despite the complexity of experimentation on NHPs as compared to non-primate species, the translational validity of NHP work remains unmatched.

### 2.3.3 Other models

While murine and NHP models are the most widely used models in biomedical imaging research with dMRI (in particular for brain applications), several other models have proven useful to the diffusion community. Examples include the pig brain, which is comparable to the human brain in myelination and development (139,140), and has been used with dMRI to study development (140) and brain lesions (141) and for tractography validation (97,138,139). Other gyrencephalic brains such as those of ferrets have been used to study psychiatric diseases, cognition and brain function with diffusion, or to validate tractography (53,142,143). Additionally, dMRI of songbirds has been used to study fundamental properties of naturally occurring neuroplasticity (144). Of particular interest, diffusion anisotropy and stroke were first experimentally observed and demonstrated in cat models (1,4,33).

## 3 Acquisition

### 3.1 Standard Protocol - overview

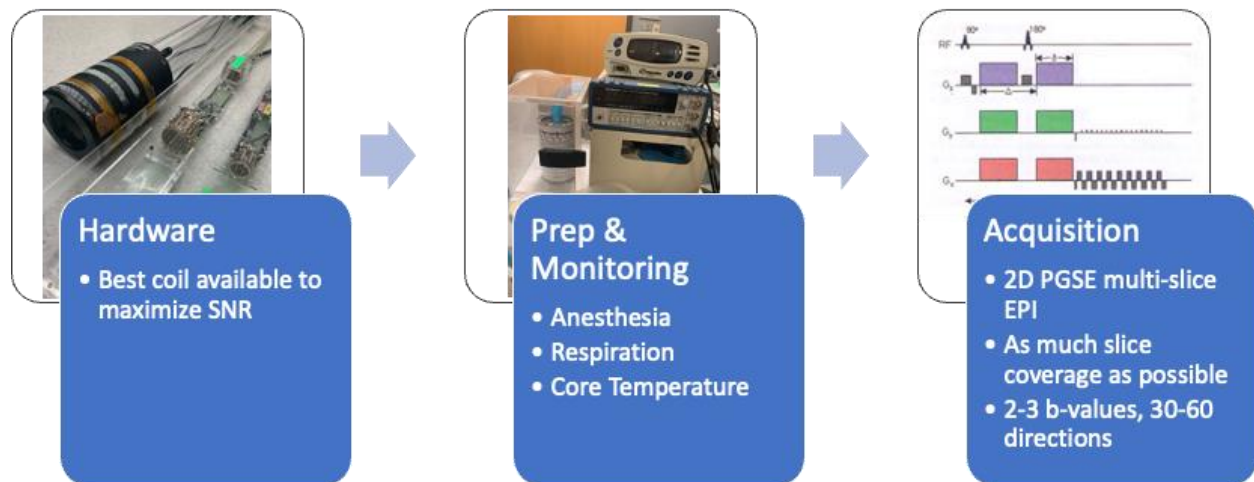


**Figure 3.** Small animal *in vivo* protocols require decisions regarding hardware, animal preparation and monitoring, and acquisition (which includes encoding, readout, spatial resolution, and  $q$ - $t$  coverage).

There are several important decisions that are made when performing dMRI of small animals, including selecting appropriate hardware, animal preparation and monitoring, and acquiring the data (**Figure 3**). In this Subsection, we present a **recommended ‘standard’ imaging setup and acquisition protocol that can be achieved in 20-30 minutes, and will be appropriate for a vast number of diffusion applications and analyses**. Naturally, if more scanning time can be allocated to diffusion MRI (vs other modalities that may be included in the protocol), will allow richer diffusion data. Ultimately, the retained dMRI protocol should be suitable for the planned analysis.

It should be emphasized that the suggestions in the current section reflect a typical protocol as a starting point for many studies, particularly those that aim to introduce dMRI to investigate animal models. Detailed information on each decision is described in the following sections, thus justifying our ‘recommendations’ above but also highlighting other strategies and decisions that may be made to optimize the diffusion acquisition for a desired experiment. Following data acquisition, recommendations for data pre-processing and processing are presented in [Section 4 - Data Processing](#).

**Hardware:** Most investigators will be limited to use the hardware available at their imaging center. Investigators should use the best combination of coils available to maximize SNR, which for many experiments will be the smallest coil that fits the animal and anatomy under investigation. Advantages and tradeoffs of using volume coils, array coils, surface coils, and cryogenic probes are discussed in [Section 3.2 - Hardware](#).

**Preparation and Monitoring:** Proper animal preparation and monitoring ensures physiological homeostasis to improve data quality and ensure animal safety and recovery. First, animals are typically anesthetized, commonly with isoflurane, a convenient, flexible and widely used anesthesia, which can be adjusted during the scan to achieve a stable respiration rate, and is cleared rapidly for prompt animal recovery. Minimal monitoring includes measuring animal respiration and temperature, since body temperature can drop under even moderate amounts of isoflurane. Brain imaging does not typically require respiratory or cardiac gating provided the head is adequately immobilized. For non-brain applications, gating strategies to limit the effects of physiological motion are typically imperative. Monitoring and gating strategies are discussed in detail in [Section 3.3](#) - *Preparation and Monitoring*.

**Diffusion sequences:** When designing the imaging experiment, decisions include selecting (1) how to encode, or sensitize, the sequence to diffusion (i.e., **diffusion encoding** — [Section 3.4](#)), (2) how the **signal readout** is performed ([Section 3.5](#)), (3) the appropriate ***q-t* coverage**, or the *b*-values, diffusion times and number of diffusion directions ([Section 3.6](#)), and (4) selecting the **spatial resolution** ([Section 3.7](#)). Our recommended imaging protocol is to utilize a 2D Pulse Gradient Spin Echo (PGSE) multi-slice diffusion-weighted EPI sequence, with as much slice coverage as possible and a repetition time (TR) of approximately 3-4 seconds. A matrix size of 96x96 or 128x128 voxels is recommended with the field of view adjusted to be slightly larger than the anatomy.

Since it is *in vivo* the selection of *b*-values is the same as *in vivo* human MRI. While many previous studies have used a single *b*-value for Diffusion Tensor Imaging (DTI) analysis, a protocol with at least two non-zero *b*-values (e.g. 1000 and 2000 s/mm<sup>2</sup>) and preferably three (1000, 2000, and 3000 s/mm<sup>2</sup>), if scan time allows, is recommended to enable DKI estimation and possibly biophysical modeling. Biophysical models are tissue-type specific and come with a variety of assumptions that should be verified. The interested reader is pointed to recent reviews covering the most popular biophysical models of diffusion in white matter, gray matter, muscle, prostate, tumor types, etc. (6,7,63,145,146). The mathematical minimum number of directions for DKI is 6 on the first shell and 15 on the second shell, but due to noise, preferably up to 30 and 60 directions should be acquired for the first and second *b*-value, respectively (147).

The SNR of the resulting image (*b*=0) should be at least 20 in the white matter for many modeling applications (148), so as to ensure an SNR  $\geq 2$  for most diffusion-weighted images at the highest *b*-value (assuming an average diffusivity of 10<sup>-3</sup> mm<sup>2</sup>/s). Further, although averaging

individual images is one way to increase SNR, it is recommended that greater numbers of unique diffusion encoding directions be obtained instead of a larger number of averages for a given direction.

An isotropic voxel size is recommended for tractography so as not to bias tract orientation to a specific spatial direction. For quantitative parametric maps (e.g. DTI, DKI, biophysical models), typical acquisition parameters allow for thicker slices than in-plane spatial resolution. The next sections justify our proposed standard protocol, while also describing alternative decisions and tradeoffs in detail.

The acquisition of a few  $b=0$  images with reversed phase-encode direction for the EPI read-out (relative to the main direction used in the diffusion-weighted dataset) is highly recommended to enable susceptibility distortion correction during data pre-processing (see [Section 4.1](#)).

## 3.2 Hardware (species/organ specific)

### 3.2.1 RF Coils

Radiofrequency coils are fundamental to image quality for any MRI exam, and coil performance and optimization is not unique to diffusion MRI studies. The primary recommendation is to utilize a transmit coil that will maximize homogeneity and a receive coil that will maximize SNR for the sample of interest, which for many experiments will be the smallest coil that fits the animal and anatomy under investigation. A wide variety of MRI coils are available for different applications, and these are also a hardware component many imaging centers may obtain through commercial sources or develop locally.

A general recommendation for *in vivo* imaging is that the combination of a **volume coil** for excitation and **surface coil** for reception can be ideal, as it ensures homogeneous excitation across the volume of interest and maximal reception sensitivity via the proximity of the surface coil to the body. For high performing, small gradient inserts, and especially at very high field strength volume transmitters can be problematic as they have to be properly shielded and decoupled from the gradient set. In these cases, a closer surface transmitter or dipole configuration can be an effective alternative. If a transceiver is to be used (i.e., a coil that does both RF transmission and reception), coils that fit close to the animal's head (for brain studies) such as head-only volume coils or surface array coils vastly outperform whole-body volume coils. For larger animals, custom head coils or organ-specific coils are recommended over body coils.

Lastly, the overall cable length from the coil to the preamplifiers is of decisive importance for SNR (see Friis' formulas for multi-stage amplification) with best performance being achieved when preamplifiers are placed directly on the receiver elements.

**Cryogenic probes** can increase SNR by a factor of 2.5 - 5 compared to standard room-temperature RF coils, but this gain is strongly dependent on the sample distance to the coil. Initial transmit/receive designs lacked transmit field ( $B_1^+$ ) homogeneity, but, as suggested above, receive-only designs in combination with a large volume transmit coil provide optimal performance. While cryoprobes are limited to small samples/animals, e.g. rodent brain, these are also the type of samples where ultra-high spatial resolution is needed since anatomical structures often scale with brain size. Cryoprobes can outperform the SNR obtained with a small surface receiver coil and bring the SNR of high-field systems (7 - 9.4 T) to the levels achieved with ultra-high-field systems ( $\geq 11.7$  T) without the penalty in relaxation times (shorter  $T_2$  and longer  $T_1$  at higher fields) and susceptibility artifacts.

Recent work by multiple teams (149–151) has demonstrated the utility of providing open source hardware designs for radiofrequency coils and holders.

### 3.2.2 Gradients

Most MRI systems are purchased with gradient hardware adequate for most studies, and dMRI investigators are limited to using these gradients. However, high-performance gradient sets may be available as custom inserts for small animal systems. Such inserts are capable of generating high field gradients with rapid switching times that tremendously benefit diffusion experiments. Our recommendation is to select the MRI system equipped with the strongest and fastest gradient system that is appropriate for the size of the *in vivo* animal imaging setup.

However, stronger gradients, particularly at higher fields, present several challenges, including calibration, gradient nonlinearities, and eddy currents. Gradients must be well-calibrated to ensure accurate gradient fields, and hence, accurate diffusion weightings. Similarly, gradient fields are typically linear at the center of the coil (isocenter), but they may deviate at further distances away. Since this is specific to the hardware and cannot be easily corrected during imaging, the gradient non-linearity can be measured and corrected during estimation of diffusion metrics, since it could cause considerable deviations in diffusivity particularly for large samples relative to the gradient dimensions. Finally, fast switching gradients induce currents in MRI hardware components, causing eddy current artifacts that must be compensated for, or corrected in processing.

### 3.2.3 Magnet & field strength

Most investigators will be limited to choices of scanner available at their imaging center. However, if given choices of multiple scanners with appropriate RF coils and gradient strength, a general recommendation is to use the scanner with the highest field strength, that has a bore (gradients included) large enough for the animal/sample to be imaged. Indeed, a higher static field strength provides substantial advantages in terms of higher SNR which can be traded for a higher spatial resolution.

However, higher fields, particularly with diffusion imaging, also come with several challenges. At higher field strengths,  $T_1$  is longer and  $T_2$  shorter. For an in-depth discussion of the physics behind the field dependence of the relaxation properties see e.g. (152). Early experimental investigations of the field dependence of relaxation were performed in frog muscle (153). Later work has provided detailed insight into the  $T_1/T_2$  variation among different brain regions at various field strengths (154). While the loss of  $T_1$  contrast is manageable, the decrease in  $T_2$  is of more consequence, as it imposes a need for short echo times and reinforces the need for strong gradients. Additionally, field inhomogeneities at higher fields may become problematic in acquisition strategies that are sensitive to local field imperfections. This poses additional challenges not only for gradient designs to allow active shim coil integration, but also for gradient power amplifier construction. Furthermore, the design of efficient active shielding and magnets in such a way that eddy currents are minimized becomes increasingly challenging for higher field strengths. For *in vivo* imaging another challenge of high field MRI is the increased RF energy deposition compared to lower fields, as well as the larger  $B_1$  field inhomogeneity due to the shorter RF wavelength, although the latter is a lesser concern for small objects of interest such a rodent heads.

### 3.2.4 Where future work should lie

Image acceleration is still very limited on pre-clinical scanners due to the low number of receiver coil elements (usually 1 - 4 for brain imaging because of the object's small size). Progress in this field would be valuable not only for reducing scan time but also for reducing artifacts such as ghosting. For example, there are alternative methods to navigators for ghost corrections that rely on reconstruction-based approaches (155–157).

### 3.3 Animal preparation & physiological monitoring

In general, maintaining stable physiological homeostasis is important for any type of *in vivo* study. MRI has the additional complication that monitoring needs to be performed somewhat remotely since the animal is placed in the magnet bore, although several vendors provide MRI-compatible and non-interfering systems. Reducing stress and physiological differences between animals helps to reduce variability which is particularly important for identifying group differences and for longitudinal studies.

A minimum monitoring setup includes respiration rate and core temperature. Monitoring cardiac rate, arterial saturation, blood gasses, blood pressure or end-tidal CO<sub>2</sub> levels may be useful, but are often not needed for studies of tissue structure. A key factor for diffusion properties and animal homeostasis is that maintenance is sufficient to prevent edema or brain swelling, and prevent whole body dehydration (a particular problem with small animals). A constant core temperature is also warranted to improve consistency of diffusivities and of T<sub>1</sub>-weighting throughout the protocol, both of which are temperature-dependent (158). A problem with diffusion studies is that the acquisition time can be quite long. A rule of thumb for a mouse is that if anesthesia exceeds two hours then support for hydration should be considered. For post-scan animal recovery, inhaled anesthetics (e.g. isoflurane) have a faster elimination through the lungs while injectable ones need to be metabolized and excreted (e.g. medetomidine). An antagonist to the latter is recommended to speed up the recovery phase for the animal (e.g. atipamezole).

Anesthetics, for example isoflurane, further have an effect on vasodilation/constriction, hypoxia and/or temperature, all of which can affect the diffusion measurement either directly (temperature) or indirectly (blood oxygenation dependent field homogeneity, variable contribution of blood pool to diffusion signal in each voxel, etc.), though the latter effects are not expected to be dramatic. Data acquired under different anesthesia conditions should however be interpreted with caution. A whole brain, quantitative increase in the water ADC has been reported with increasing anesthetic agent dosage for both isoflurane and medetomidine, two of the most commonly used anesthetics (159). Moreover, not all brain regions exhibit the same ADC increase with both agents. Under isoflurane, the ADC increase pattern encompassed more regions than with medetomidine. At the level of the entire brain, the ADC values measured under medetomidine are typically lower than those measured under isoflurane anesthesia. Recently, advantages in the physiological properties of dexmedetomidine over its racemat medetomidine have been reported and large animal laboratories have started converting their anesthetic

protocols (160,161). When comparing the ADC measured in awake and isoflurane anesthetized mice (162) no significant differences.

### **Physiological Gating**

Since diffusion is sensitive to microscopic motion, bulk motion due to respiration or cardiac pulsation is a particular concern. Diffusion imaging of the brain does not typically require respiratory or cardiac gating provided the head is sufficiently stabilized within an appropriate holder which for rodents includes both teeth and ear bars. For non-brain applications, gating strategies to limit the effects of physiological motion are typically imperative. For control of respiratory motion, it is important to acquire images during the quiescent period of the respiratory cycle, although not all vendors provide this setup and custom solutions may be necessary for acquiring 'burst-mode' type acquisitions (163) that rearrange delays and acquisitions to minimize artifacts. Furthermore, respiratory gating also needs to be balanced with any potential effects on critical timings such as repetition time (TR). For most diffusion scans, TR is sufficiently long that respiratory delays do not considerably affect image contrast provided the animal is stable throughout the duration of the experiment.

### **Where future work should lie**

Systematic reporting of animal monitoring and anesthesia procedures as well as the resulting physiological measures (e.g. respiration rate and core temperature) in dMRI publications can contribute to improved reproducibility or multi-site comparison of results. Recent work also demonstrates the feasibility of awake rodent MRI removing the need for anesthesia and reducing the need for monitoring. It has been shown that habituation can be achieved even for long scan sessions although animal sex must be taken into account in the habituation procedure (164).

## **3.4 Acquisition: diffusion encoding**

A number of possible **diffusion encoding**, or sensitization, schemes are shown in Figure 3 (left). Most diffusion-weighted sequences trace their origin to the pulsed gradient encoding scheme pioneered by Ed Stejskal and John Tanner in 1965 (165). Here, strong diffusion-sensitization gradients are applied on either side of a 180° refocusing pulse, hence, this encoding is typically referred to as the **pulsed gradient spin echo (PGSE)**. PGSE offers a mathematically elegant way to quantify diffusivity, gives access to a biologically relevant range of

diffusion times (e.g. 10-50 ms on a preclinical MRI system at high field) and a broad range of  $b$ -values (e.g., 0—12,000 s/mm<sup>2</sup>). For this reason PGSE has become the most widely used diffusion encoding strategy in both human and animal imaging, and is the “default” encoding scheme on all current scanners.

However, a number of alternative diffusion encodings are possible, particularly on preclinical systems. Here, researchers have an easier access to modify the way diffusion-weighting is played out, and cutting edge research and modeling may require more elaborate schemes than PGSE. Stronger gradients can take a variety of shapes, enabling sensitivity to different anatomical features. For this reason, there is no “consensus” on the best encoding strategy, and depending on time constraints and the ultimate research goal, different encoding may be optimal. Instead, we describe the pro’s and con’s of various encoding schemes, and when possible, suggest guidelines when using these sequences.

In some instances, a researcher may be interested in probing very long diffusion times - for example to investigate changing length scales, increase diffusion weighting, or possibly investigate diffusion restrictions in other tissues/organs with different microstructure than the brain. Here, a **stimulated echo acquisition mode (STEAM)** sequence for encoding may be useful. In a traditional spin echo sequence, a longer diffusion time leads to a longer TE, and a consequently lower signal. STEAM sequences aim to overcome this by decorrelating the diffusion time from the echo time (166). The diffusion weighting gradients are played before and after two 90 degree pulses, storing the magnetization in the longitudinal plane for a period of time. Thus, STEAM preparation is limited by  $T_1$  recovery rather than by  $T_2$  decay. Longer  $T_1$ ’s at high field thus enhance the possibilities of STEAM. The downsides of STEAM are lower SNR compared to PGSE (for equal echo times) and larger contributions from imaging gradients to the diffusion-weighting via cross-terms. This aspect makes the calculation of the effective  $b$ -value mandatory as it can differ substantially from its nominal value, and potential issues with large variations in effective  $b$ -values across directions over the same “shell” (167).

On the other end of the diffusion time spectrum, **oscillating gradient spin echo (OGSE)** (168) can be used to assess much shorter time and length scales (0.1-10ms). As the name implies, pulsed gradients are replaced with periodic sinusoidal gradients. The effective diffusion time of the experiment is then related to the period of oscillation, which can be tuned to be very short. This comes at the cost of modest attainable  $b$ -values, and a higher risk of nerve stimulation due to rapidly switching strong gradients. The  $b$ -value can be increased by lengthening the sinusoidal waveforms, enabling short diffusion times with moderate diffusion weightings.

In the above-mentioned schemes, the signal is sensitized to diffusion along a *single* spatial direction defined by the diffusion gradients. As such, this sequence can often be referred to as a **single diffusion encoding (SDE)** experiment. This nomenclature has become popular in recent years to contrast with techniques, **multi-dimensional encoding (MDE)**, which encode diffusion by using multiple sets of diffusion encoding gradients along (possibly) different directions. MDE examples include double diffusion encoding (DDE) (169,170) or triple diffusion encoding (171,172), where two (or three) pairs of pulsed gradients are separated from each other by a mixing time  $t$ . This increases the dimensionality of possible controllable parameters, and enables probing microscopic anisotropy (by varying the relative orientation of gradients (173,174), compartmental kurtosis (by varying gradient strengths of orthogonal gradients (175), or compartmental exchange (by varying mixing time of parallel gradients (176–178). Further, free gradient waveforms may be designed which enable similar investigations into diffusion microscopic anisotropy, structure size variance, and orientational coherence, and is often referred to as  $q$ -trajectory imaging (QTI) (179). Disadvantages of these sequences include potentially longer acquisition times, long echo time, ill-defined diffusion times, or complicated modeling and analysis. For a review of multidimensional diffusion encoding see (172).

Other encoding techniques include **steady-state free-precession (SSFP)** with a diffusion preparation (180,181). SSFP acquisitions are essentially a rapid train of repeat pulse-encode-readouts (182), enabling sampling and readout in tens of milliseconds, and greatly increasing the potential to achieve efficient diffusion weighting because of the greatly increased fraction of time spent acquiring signal. While strong, efficient diffusion weighting is possible, SSFP suffers from requiring a segmented readout (making it susceptible to motion artifacts), sensitivity to field inhomogeneity which leads to banding artifacts, and a complicated signal dependence on  $T_1$ ,  $T_2$ , and flip angle which makes diffusion quantification difficult. Despite this, diffusion-weighted SSFP has been heavily utilized *ex vivo*.

An alternative to SE sequences is to employ diffusion weighted **gradient echo (GE)** sequences (183,184). An important advantage of such acquisitions is the ability of using small flip angles and short TR, which provide a substantial decrease of the acquisition time in high resolution 3D acquisitions. However, a disadvantage at high field is the increased susceptibility artifacts.

Because of the strong preclinical gradients, eddy currents can create artifacts in diffusion images. It is possible to modify the diffusion encoding to a twice-refocused spin echo, consisting in a set of encoding and refocusing gradients that will act to cancel out eddy currents from the

pulse gradient prior. Thus, this **eddy current nulled (ECN)** encoding can minimize these artifacts, although at the cost of decreased encoding efficiency and a longer TE.

Clearly, there are many ways to encode diffusion into MRI images. With tradeoffs in diffusion times, diffusion weightings, sequence time, microstructure sensitivity, and artifact sensitivity, the optimal encoding strategy ultimately depends on the experimental question and desired application. Some non-standard diffusion weighted preparations, for instance using multiple gradient echoes or multiple spin echoes, as well as the respective data reconstruction/analysis pipelines are provided in the REMMI toolbox (<https://remmi-toolbox.github.io/>) for different vendors.

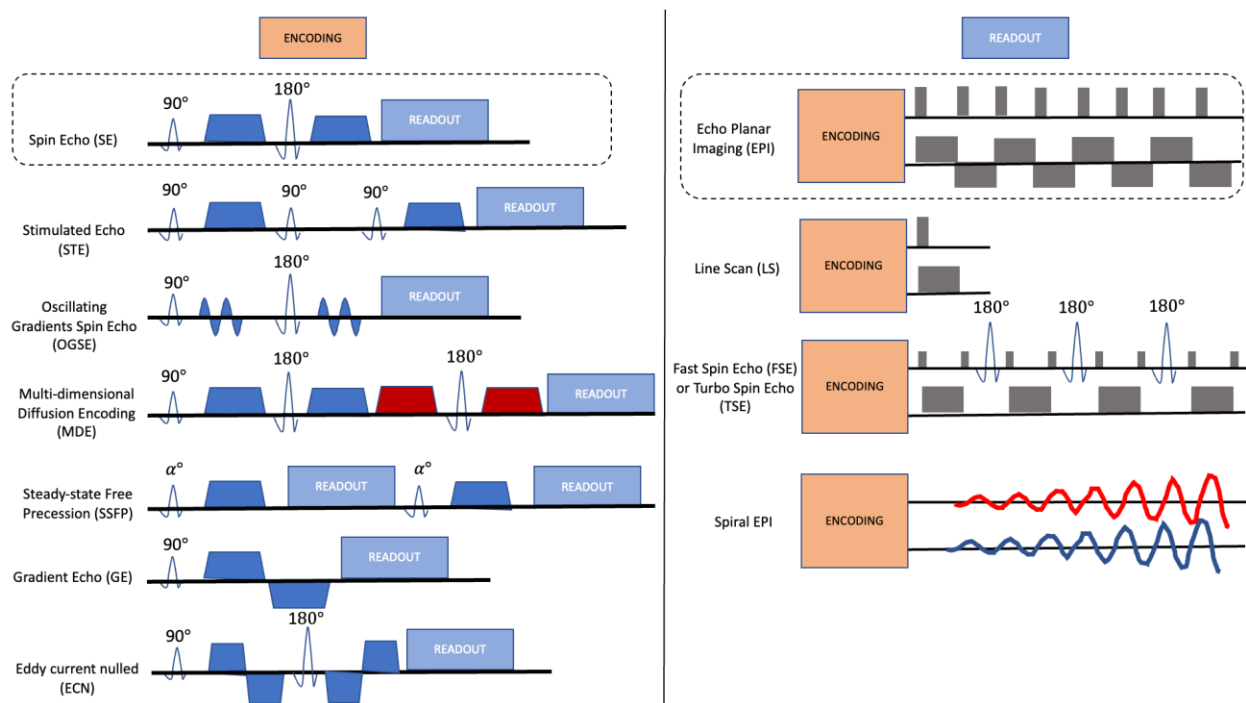


**Figure 4.** Diffusion encoding and readout. Pulse sequence diagrams are shown for a variety of representative encoding (Section 3.4) and Readout (Section 3.5) schemes.

### 3.5 Acquisition: signal readout

After the diffusion encoding, the **signal readout** module is played out (**Figure 4**, right). For most diffusion MRI sequences, this is typically an **echo planar imaging (EPI)** readout using rapidly oscillating phase/frequency gradients generating multiple gradient echoes. This rapid acquisition minimizes effects of bulk motion on the diffusion images, and acquires images in a single excitation to minimize the scan time needed to acquire many diffusion volumes. The EPI readout is also compatible with all diffusion encodings above, except SSFP. For these reasons,

a **single-shot multi-slice pulsed-gradient EPI sequence** has become the most popular in humans, and is also our recommended starting point for small animal *in vivo* imaging.

While EPI reduces scan time and motion artifacts, it also faces its own challenges, most prominently susceptibility distortion due to  $B_0$  field inhomogeneity that causes not only geometric warping but also signal intensity stretching and pileup. This can be especially challenging at high field strengths, and when acquiring large acquisition matrix sizes (for high spatial resolution or field of view), typical of preclinical imaging. To alleviate this, it is possible to acquire data with a segmented readout, where  $k$ -space is read out in multiple shots. This comes at the cost of increased scan time and possible ghosting artifacts due to physiological motion that are typically corrected for using phase navigation techniques. Another alternative consists in taking advantage of partial Fourier acceleration in the phase direction, at the expense of the SNR and blurriness depending on the reconstruction algorithm for recovering the missing  $k$ -space lines. Finally, acquiring additional reversed phase-encoded  $b=0$  images can help in compensating geometrical distortions during image preprocessing (see [Section 4.1.1](#)).

Other readouts are also possible for small animal *in vivo* imaging. For example, a **rapid acquisition with relaxation enhancement (RARE)**, sometimes called **fast spin echo (FSE)** or **turbo spin echo (TSE)**, is composed of multiple RF pulse echo trains and allows collection of multiple lines of  $k$ -space in a single excitation (typically factors of 4-12). RARE sequences are less prone to susceptibility induced artifacts than EPI, and offer a good tradeoff between scan time and image quality, especially for smaller specimens. (89,185). Similarly, the **gradient and spin echo (GRASE)** readout allows for further acceleration with the acquisition of additional phase  $k$ -space lines by generating gradient echoes on each side of the RARE spin echoes. Additionally,  $k$ -space can be sampled in a **spiral readout** rather than cartesian readout. Spiral acquisitions have several advantages including the possibility to sample the center of  $k$ -space at the start of the echo and minimizing TE, and also the ability to perform either single shot or multi-shot readouts. This readout remains nonetheless sensitive to  $B_0$  field inhomogeneities and eddy currents (yielding geometric distortions) in the higher spatial frequencies. While this complicates artifact correction after image reconstruction, eddy currents can be minimized via trajectory measurements (186).

### 3.6 Acquisition: $q$ - $t$ coverage

There is certainly no recommendation on an “optimal”  $q$ - $t$  coverage, which is highly dependent on the microstructure feature one wishes to maximize sensitivity to (187). As

mentioned, because it is *in vivo* the  $q$ - $t$  coverage follows that of *in vivo* humans. Before setting up the diffusion parameters, it is important to understand if there are any theoretical requirements of the model or data analysis framework which will be used downstream, such as short gradient pulses (to be in the narrow pulse approximation), short / long diffusion times,  $b$ -value regime etc. and to acquire data that suits the theoretical foundation of the analysis framework. In general, on preclinical systems there is a lot of flexibility in choosing the sequence parameters which is very handy for optimisation strategies. We recommend acquiring non-diffusion weighted images ( $b=0$ ) at approximately a ratio of one image for each 10-20 diffusion-weighted images (147,188).

Below we provide guidelines for common applications: signal representations (DTI/DKI), tractography and biophysical models.

**DTI** is by far the most widespread analysis of dMRI data. The acquisition guidelines are similar to those for human studies. One non-zero shell with 6 non-collinear directions is the mathematical minimum to estimate a diffusion tensor, but since more directions are beneficial to mitigate the effects of noise and anisotropy, 20 – 30 directions are usually acquired. To maximize precision, the  $b$ -value should be chosen such that the signal decay is substantial, e.g. such that  $bD \approx 1$ . *In vivo*, the most standard  $b$ -value is  $b = 1000 \text{ s/mm}^2$ , as in humans. The  $b$ -value can be adapted based on the animal's body temperature, e.g. songbirds have a higher body temperature (40-41°C in normal conditions), leading to the use of lower  $b$ -values for DTI.

**DKI** is an extension of DTI that also estimates non-Gaussian characteristics of water diffusion in biological tissues (diffusion kurtosis), as an empirical measure of tissue heterogeneity, i.e. how much the tissue differs from a Gaussian medium with matching diffusivities as derived from DTI. The acquisition guidelines are also similar to those for human studies. Two non-zero shells with 21 (6 + 15) non-collinear directions is the mathematical minimum to estimate the diffusion and kurtosis tensors, but 20 – 30 directions per shell are usually acquired (189). To maximize precision while staying within the radius of convergence of the cumulant expansion (190), the highest  $b$ -value should be chosen as  $b \approx 2000 - 2500 \text{ s/mm}^2$  *in vivo*. Often the rule of thumb  $b_{max} < 3/DK$  can be used, as from this point on the DKI signal expression starts to increase with increasing  $b$ . (191) comprehensively optimized the experimental design for DKI by minimizing the Cramér–Rao lower bound of the DKI parameters. The optimized scheme consisted of four shells at  $b = 0, 700, 1200$  and  $2800 \text{ s/mm}^2$ , with the number of  $q$ -space samples per shell increasing with  $b$ -value. Their optimized set was benchmarked on *in vivo* data from both a human and a rat brain. The same set was also used for *in vivo* mouse brains in the context of fiber tracking using multi-tissue constrained spherical deconvolution where the multiple  $b$ -values allowed good CSF/GM/WM segmentation and the large number of  $q$ -space samples at the outer

shell allowed good fiber orientation estimation (192). It is important to note that DTI is inherently contained in the DKI framework and moreover that DKI provides more accurate estimates of DTI parameters than DTI on its own (193). Given recent advances in acquisition efficiency and speed, we advocate the new minimal acquisition to become two-shell data (as opposed to widespread single shell) and thus the DKI analysis to become the new “default” over simple DTI. The overwhelming advantage of both approaches is that, unlike biophysical models, they rely on an empirical representation of the diffusion signal and make no assumptions about the underlying microstructure or properties of the tissue (6). They are thus widely applicable to any situation, with kurtosis providing complementary information to first-order diffusivities. Note, however, that optimal DKI design may depend on the target tissue and that processing affects DKI estimates substantially (194). For this reason, it may be beneficial to use highly sampled repository data sets for study planning (195). For reduction in DKI scan time, strategies for “fast kurtosis” estimation decrease the minimal number of measurements needed (196,197) axial symmetry of diffusion properties in the voxel, these methods can also provide metrics of white matter architecture (198). The fast kurtosis methods are reviewed in (199).

**Guidelines for  $q$ - $t$  tractography:** Today tractography methods appear to be less sensitive to the selection of scan parameters ( $b$ -values, number of gradient directions) than choices in the tractography pipeline itself, including fiber orientation reconstruction technique, tractography methodology and algorithms for streamline propagation, seeding strategies and exclusion criteria, and bundle segmentation procedures. This has been shown in both humans and animal (typically *ex vivo*) studies (131,136,200–204). Our recommended protocol for  $q$ - $t$  tractography includes 50–60 directions at a moderate-to-high  $b$ -value. For most methods that estimate fiber orientation, this scheme has proven adequate to accurately estimate fiber orientation distributions (205), and this is expected to hold in animals as in humans, although differences in fiber complexity are expected. This protocol is also compatible with tools such as ‘tractogram filtering’ and ‘microstructure-informed’ tractography (206–211) which attempt to enable a quantitative assessment of structural connectivity, or connection density, by linking local voxel-wise microstructure measures with the global and multi-voxel nature of streamlines.

Guidelines for acquisition in the perspective of **compartment modeling** analysis are generally the same as in humans, with one nuance: preclinical scanner hardware may allow the exploration of regions of  $q$ - $t$  space that are not achievable on clinical systems, in terms of high  $b$ -values and/or short diffusion times. Thus, the data requirements of some biophysical models may be better met for small animal imaging than human imaging.

Shorter diffusion times are typically favored or enforced when special effort is put into minimizing the echo time – to account for shorter  $T_2$  at high field. These differences may pose additional challenges when extrapolating results obtained in small animals to humans. We therefore underline how important it is to report the diffusion time as part of the acquisition parameters, even when the diffusion time dependency is not the focus of the study, particularly in small animal imaging. Indeed, the diffusion metrics measured in one study may differ from another study if different diffusion times were used, depending on the tissue microstructure of interest and disease. As mentioned earlier, diffusion metrics measured at typically short diffusion times (10 - 20 ms) in preclinical experiments can be different than those measured in clinical studies with substantially longer diffusion times (typically longer than 50 ms) because they will be sensitive to different aspects and spatial scales of the micro-environment.

In fact, preclinical scanners offer a unique opportunity to investigate diffusion time-dependence of diffusivity  $D(t)$  or kurtosis  $K(t)$  over diffusion time ranges that are difficult to achieve on clinical systems (in particular, short diffusion times either using OGSE or PGSE), concomitantly with the exploration of high  $b$ -values (19–21,212–216). For studies with short to intermediate diffusion times (up to ~40 – 50 ms) we recommend to keep the echo time constant to a value which allows for the longest gradient separation ( $\Delta$  in a PGSE scheme). Indeed, except for a combined diffusion – relaxometry model, accounting for variable  $T_2$ -weighting considerably complicates the data analysis. We underline this constant TE recommendation as it is commonly (and unfortunately) not the primary choice due to SNR considerations. For longer diffusion times (>80 ms), a stimulated echo sequence can be used, but in that case the effect of the cross terms needs to be accounted for (effective  $b$ -matrix /  $b$ -value, or explicit imaging / crusher gradient duration and strength when modeling restricted diffusion) (167,217) – see below.

### **Other practical considerations.**

For studies including the acquisition of multiple  $b$ -values, it may be convenient to randomize the order of the acquisition of the DW images, so that blocks of highly DW measurements are not acquired at once. Interspersing weaker and stronger diffusion weighting minimizes the risk of gradients overheating and reduces the duty cycle.

For high field strengths, the RF energy deposition may cause heating of the sample which can be substantial for short TRs and compromise the temperature stability required for usable dMRI data. A temperature steady-state may be eventually reached but transients will be present in the beginning of the scan. Interspersed  $b=0$  images are a very effective way of controlling for these effects, scanner stability and image quality throughout long acquisitions (218). A slow drift

in  $b=0$  amplitudes across time can be corrected for instance using a linear detrending, applied to all diffusion-weighted images. When diffusion data is acquired in multiple experiments, it is also important to ensure that the adjustment parameters (reference power, receiver gain, etc.) are consistent, ideally by preventing them from being updated between scans.

It is recommended to optimize the distribution of diffusion-encoding directions, as done for humans dMRI. Directions should be distributed across all shells (i.e. using electrostatic repulsion within and between shells) and should cover the full sphere instead of the half-sphere (147,188). This coverage is optimal unless there is a specific need to acquire the same directions on each shell, for directional fits of diffusivity and kurtosis for instance. The recommended schemes cannot usually be generated by the vendor software and should be generated separately and imported into the system as a custom gradient direction file — (see [Section 5.1](#) on open sourced resources, and <https://github.com/ecaruyer/qspace>, in particular).

For any dMRI analysis in general, it is also crucial to use the effective b-matrix, not just the nominal one that was entered as the input scan parameters. The effective b-matrix is typically provided in an output file collecting all acquisition parameters. For non-vendor sequences, this may not be supported and the effective b-matrix needs to be calculated directly using the sequence diagram and all known gradients played in the sequence. Ice water (219) and other pure liquids, particularly those with low diffusivities (see Table 1 in (220)), can be useful phantoms to assess whether the correct b-matrix is used. Such phantoms can also be used to measure the effect of gradient spatial non-linearity on the effective b-matrix across the whole imaging field, as well as to test for spurious “diffusion time-dependence” from scanner drifts, etc. It is also recommended to include the effective b-matrix when reporting methods, to improve between-site comparisons and thus increase the value of animal study results toward clinical translation and validation.

The short pulse approximation ( $\delta \ll \Delta$ ) can usually be achieved in preclinical MRI and micro-imaging (MR microscopy). As a result, the data are acquired under conditions that agree with most analysis frameworks. This however, is not the case for clinical MRI where diffusion gradients are not as strong and pulse lengths are longer as a consequence. This may pose a problem when translating findings from preclinical studies using advanced analysis frameworks built on the short pulse approximation to interpret clinical dMRI findings. If the diffusion data are used for estimating microstructural feature sizes (e.g. soma size), the estimation of the latter is more accurate when the diffusion gradient duration is accounted for, even if the narrow pulse approximation holds.

With high field strengths and associated field inhomogeneity, proper  $B_0$  field shimming becomes critical. Global first order shimming on the entire coil-sensitive MRI volume — such as the automated shimming procedure available at the console — can be a good start for this purpose, while higher order shimming in the targeted imaging volume improves image quality substantially. Higher order shimming can be achieved using either methods directly available as products (e.g. MapShim on Bruker or FastMap on Varian), or using in-house developed routines (e.g. several groups have their own implementation of FastMap ([Rolf Gruetter and Tkac 2000](#); [R. Gruetter 1993](#))).

### **Where future work should lie**

Pre-clinical MRI vendors are encouraged to implement diffusion product sequences where the default direction sampling is full sphere (rather than half-sphere, see comments on eddy current correction later), and open the possibility for multi-shell acquisitions with different directions across different shells. Default randomization of the order in which  $b$ -values and directions are acquired would also constitute an important improvement, as well as distributing  $b=0$  acquisitions throughout the scan, to control for drifts, temperature changes and/or physiological effects.

The harmonization of DTI acquisition protocols (e.g. as to the choice of a maximum  $b = 1000 \text{ s/mm}^2$  *in vivo*) may help multi-site reproducibility and comparison studies. Notwithstanding, encouraging the community to acquire richer datasets by default (e.g. multi-shell at minimum, but even for multiple diffusion times) can open up many avenues for testing new models retrospectively on public datasets, in a variety of animal models, healthy and diseased.

The development of biophysical models of tissue should uphold high standards in terms of accuracy and precision of microstructural features estimated, and validated using complementary techniques such as light microscopy.

Finally, the flexibility associated with preclinical MRI scanners will hopefully foster further developments in terms of novel diffusion encoding and acquisition techniques to bring dMRI ever closer to *in vivo* histology.

## **3.7 Acquisition: Spatial resolution**

The image spatial resolution is a critical decision in any experimental process. Although brain dimensions vary by orders of magnitude across species from the mouse (0.4mL) to human (1300mL) the relative size of voxels to the size of the brain are generally consistent across many

species. Put simply, spatial resolution is a balance between the available SNR and scan time, thus, resolution should be as high as permissible for the targeted SNR and scan time.

Depending on the application, it may be recommended to acquire voxel sizes that are isotropic instead of resolutions with considerable differences between the in-plane resolution and slice thickness, though the latter is a more widespread design. Indeed, for interpretation of morphological details and anatomical boundaries, high-resolution, isotropic voxels are important since inspection in multiple planes of orientation facilitates interpretation, and thick slices will introduce partial volume effects that are more difficult to control. Non-isotropic resolution may further lead to undesired effects if image registration is performed at any stage in processing. However, isotropic voxels may not be a necessity in many experiments, and allowing thicker slices is both faster and less gradient demanding, while yielding higher SNR.

Naturally, there is no single set of guidelines, or consensus, on image resolution for specific species. Rather than providing specific recommendations for resolution, below we give typical volumes of brains, and compute what the equivalent voxel size (i.e, the **volume equivalent resolution**) would be given the ratio of volumes, and a typical 2-mm isotropic human scan (assumed approximately 1260 mL volume). We have chosen 2-mm isotropic as a ‘standard’ only for comparison purposes, and note that larger voxel sizes (2.5-mm or 3-mm isotropic) are common, and smaller voxels are also possible with novel acquisition strategies (221–224) or stronger gradients (<1-mm isotropic).

### *Volume equivalent resolutions and pushing the boundaries*

**Table 1** provides an overview of the brain volumes of most common species, with matching spatial resolutions to the typical human dMRI resolution (e.g., a mouse brain with a volume at 0.4mL scanned at 140um isotropic resolution matches a human brain with a volume of 1200mL scanned at 2mm isotropic resolution based on matching of volume-to-volume ratios), and ranges of spatial resolutions reported in the literature, *in vivo*.

Similar figures hold for other mouse organs used in dMRI literature, such as the liver (112). For example, for an approximate mouse liver volume of 2.5 mL and human liver volume of 1600 mL, mouse liver MRI resolutions of 250 μm would have a similar volume ratio as a human liver scan performed at 2mm resolution.

Species	Brain Volume (mL)	Matching spatial resolution (isotropic)	Reported in literature ( <i>in vivo</i> )

Human	1200	2 mm	1 — 3 mm isotropic
Mouse	0.4	140 $\mu\text{m}$	100 — 200 $\mu\text{m}$ in-plane 200 — 300 $\mu\text{m}$ slice thickness “Extreme” datasets: 75 — 125 $\mu\text{m}$ isotropic
Rat	0.6	160 $\mu\text{m}$	100 — 300 $\mu\text{m}$ in-plane 250 — 600 $\mu\text{m}$ slice thickness
Squirrel monkey	35	600 $\mu\text{m}$	600 — 700 $\mu\text{m}$ in-plane 1 mm slice thickness
Macaque	80	800 $\mu\text{m}$	500 $\mu\text{m}$ — 1 mm in-plane 1 — 2 mm slice thickness “Extreme” datasets: 580 $\mu\text{m}$ isotropic

**Table 1.** Summary of brain volumes of various species, matching spatial resolutions to the typical one for human dMRI, and ranges of spatial resolutions reported in the literature, *in vivo*. A few references are provided, but are by all means not comprehensive. Resolutions reported in literature taken from (225) (human), (12,71) (mouse), (94,214) (rat), (226) (squirrel monkey), (13,227,228) (macaque).

## 4 Data Processing

In this paper we refer to *pre-processing* as steps that come before any diffusion fitting (tensors, biophysical models, etc.). Pre-processing thus includes data conversion (e.g. DICOM to NIfTI), noise reduction, artifact correction/mitigation or any step that aims at improving data quality. Processing refers to diffusion data fitting and normalization to standard space. See **Figure 5** for flowchart.

### 4.1 Pre-processing pipeline

The minimum recommended steps for data pre-processing include debiasing, reduction of thermal noise (referred to as denoising), unringing, signal drift correction, and combined eddy-current distortions, sample/animal motion, and susceptibility distortion correction using open-source or freely-available software packages as described below and recapitulated in [Section 5.1](#) - *Open Science*. For studies of microstructure, diffusion kurtosis imaging metrics are recommended along with diffusion tensor metrics in both processing and reporting.

### 4.1.1 Brain

Generally, pre-processing diffusion datasets of preclinical acquisitions is similar to that of the *in vivo* human brain. Below we detail the steps associated with a typical pre-processing pipeline, stressing in particular what may differentiate *in vivo* human brain from small animal implementations, and how available tools can/should be adapted accordingly.

For data importation and reconstruction it is critical that the observable MRI signal is properly organized in *k*-space and transformed into the image domain. Note that image reconstruction is typically done at the console by the vendor software. Additionally, an image matrix by itself is not sufficient, and there must be an image header, or a separate text file, that contains information about spatial resolution and sample orientation, in addition to desired image sequence parameters. DICOM, NIfTI, Minc, Analyze, among others offer standardization. Pre-clinical scanner software often outputs data in their own vendor-specific format. Recent scanner software versions offer the possibility to export the data as DICOM or NIfTI directly, though sometimes omitting important metadata such as diffusion gradient directions. Overall, explicit conversion by the user to one of the aforementioned formats - typically using in-house written code - is still widespread, which entails possible incompatibilities with BIDS format, data sharing and processing multi-center data. Some solutions such as DICOMIFIER (229) exist, and the adoption of a standard tool by the community - or by the vendors - will greatly aid data harmonization.

Finally, the definition of diffusion gradient directions may not be consistent across vendors or across in-house written data conversion pipelines, with some given in the “imaging frame” i.e. in relation to readout, phase encode, slice direction or PE2 and others in the “lab-frame” with Z being typically along the direction of the main magnetic field. The orientation of the images with respect to the applied diffusion directions is very important, particularly for tractography, and should be checked carefully. Tools are also available to systematically correct any errors (230,231).

In the perspective of increasing data sharing opportunities, as well as generating traceable and comparable datasets, we strongly encourage organizing raw pre-clinical data using the BIDS format.

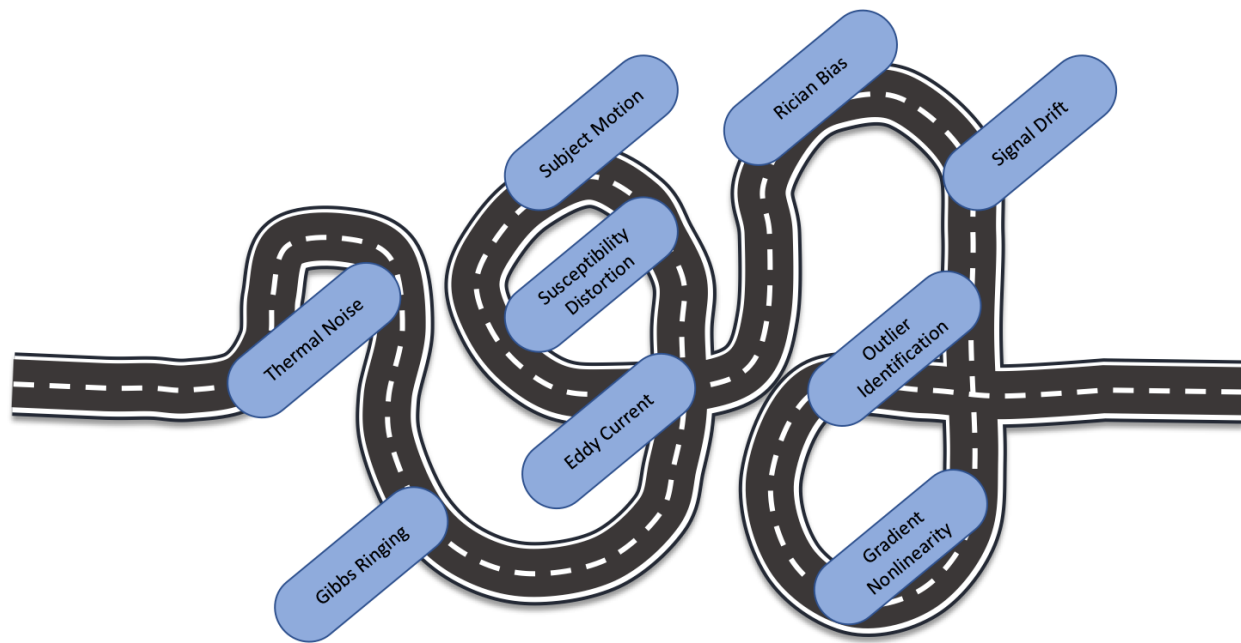


**Figure 5.** Roadmap to correcting dMRI artifacts is tortuous. As for *in vivo* human diffusion imaging, it is important to mitigate, reduce, or correct for these. Note that the “winding” road is intended to emphasize that these are not necessarily presented in order, and correction may not be necessary in all cases. Nevertheless, the most common order for pre-processing steps is: (i) Thermal denoising, (ii) Gibbs ringing correction, (iii) Susceptibility distortion + motion + eddy current corrections (+ gradient non-linearity, if applicable), (iv) Rician bias correction and (v) Signal drift correction.

The recommended data pre-processing pipeline includes: thermal noise reduction (“denoising”) (232), Gibbs ringing correction (233–235), combined eddy-current, motion and susceptibility distortion correction (236), Rician bias correction and signal drift correction (218,237). Recent examples of the concatenation of these processing steps into a pipeline is DESIGNER and PreQual (238,239), or the pre-processing implementation in MRTrix3 (240).

Here we briefly recapitulate a few common pitfalls or quality check tests for each of these pre-processing steps, but we refer the reader to the initial papers cited above for a comprehensive description of the techniques and their realm of applicability.

The very first prerequisite for most of the pre-processing steps is providing a **brain mask**, either to save computation time by excluding non-brain voxels from the analysis or for optimizing which areas of the image to focus on. Unfortunately automated brain masking is a weak spot of non-human brain preprocessing pipelines. This can be the consequence of either algorithms using inappropriate priors for non-human brain anatomy in atlas-based brain masking (e.g. very different shapes between human and rodent, or using spatial information that includes physical dimensions and thereby failing for brains much smaller than human), or a consequence of bias

fields (inhomogeneous  $B_1$  excitation field) which strongly affect the performance of intensity-based brain masking. Bias field correction on a  $b=0$  image can be performed with a variety of software, but should be used for the sole purpose of brain extraction and not as input for the remainder of the pre-processing and processing pipeline. Dedicated tools to perform brain extraction using registration to a matching species atlas are also available (e.g. <https://github.com/jlohmeier/atlasBREX> (241)). If an atlas database for the species and MR contrast of interest is available, the multi-atlas label fusion segmentation approach performs very well (242,243). More recently, deep-learning-based frameworks have been developed and validated to identify the MR image boundaries of the brains of rodents and non-human primates (244–246). Finally, while masking the region of interest (typically the brain) may be needed at a very early stage to cut unnecessary computation time, it may/should be repeated with different settings in the final stage of pre-processing. Indeed, in the early stage the brain mask could be inflated to yield a generous brain inclusion, making sure it encompasses distortions and motion that have not yet been corrected. At the end of the pipeline, a second, more refined brain masking may be performed. When preprocessing brains from species containing sparser white matter structures (e.g. avian species), expanding the brain mask to include the skull until completion of pre-processing and normalization often yields a superior registration outcome.

**Denoising** is an image preprocessing step that reduces thermal noise in the diffusion-weighted images. If the diffusion-weighted data shows a high degree of redundancy, then a principal component analysis can be used to denoise a 4D stack of diffusion-weighted images without removing anatomical detail or edges (247). The differentiation between signal- and noise-carrying principal components has recently been automated to promote ease-of-use and robustness by adopting principles from Random Matrix Theory (232). This particular technique requires that (a) the noise level is constant across all diffusion-weighted images and (b) that the number of diffusion-weighted images is large - the suggested use is 30 images or more. If such requirements are not met, then alternative denoising strategies are presented. Various supervised, unsupervised, and self-supervised machine learning-based techniques have recently been developed and evaluated for the denoising of such data (248).

The implementation of **Gibbs ringing correction** has a large positive impact on microstructure model estimates, where the “corruption” of voxels by neighboring CSF can change the apparent microstructure composition dramatically, but has very little impact on the estimation of the fiber orientation distribution for tractography purposes, for instance (233,249,250). One common limitation is the use of partial Fourier for the acquisition, which makes the correction as implemented by (233) largely ineffective. A new approach for this correction in partial-Fourier data

has been recently developed (234); both these methods are suitable for 2D multi-slice acquisitions.

The 'topup' and 'eddy' tools in FSL, which can correct for **susceptibility distortion, eddy current or motion-related jitter** all at once require two specifics of data acquisition that are often not the default on pre-clinical scanners. On the one hand, for susceptibility-distortion correction (often needed for *in vivo* EPI-based acquisitions and essential when imaging avian/reptilian species with pneumatized bones), a few  $b=0$  images with reversed phase-encode direction should be acquired to enable the calculation of the distortion field. If these images are not available, alternative distortion correction methods might include nonlinear registration to undistorted anatomical images, or correction using a fieldmap ( $B_0$  map), if available. The latter is however less accurate if a long time has elapsed between the field map acquisition and the diffusion data acquisition. On the other hand, for eddy current correction, 'eddy' requires diffusion directions that are distributed over the entire sphere, and not the half-sphere, as may be the default in vendor product sequences. In this case, a custom diffusion direction file should be provided for the acquisition. Here,  $b$ -values should be "shelled". Because of stronger imaging gradients for small animal and *ex vivo* imaging, the effective  $b$ -values may vary quite substantially across directions within a shell, to the point that the software may not recognize them as shelled anymore. This can be overridden though by a special flag in the command line. Finally, it is important to note that parameters may need to be tuned to the sample of interest, for example the resolution or knot-spacing of warp fields for topup, or any parameters that are dependent upon spatial scale.

**Rician bias correction** consists in correcting the diffusion signal decay by subtracting the non-zero Rician floor. Typical methods will assume the Gaussian noise standard deviation to be known, for example as previously estimated using MP-PCA on low  $b$ -value data. For software and methods, see (238,251) and Section 5.1.1]. One substantial advantage of preclinical MRI data is that coils are often single-channel or quadrature recombined, and the complex-valued data is more easily retrievable from the scanner - as opposed to clinical MRI data where most often only the magnitude is exported and researchers need to retrieve individual channel raw data from 16+ channel coils and perform the entire image reconstruction themselves if they want to access complex-valued data. Complex-valued data from a single-channel coil is by design characterized by Gaussian noise. Rician bias can be thus minimized by denoising in complex space, and possibly also circumvented entirely by working with real-valued data after phase unwrapping (252).

Finally, **temporal instability** on the scanner can cause signal drift, especially for diffusion sequences where strong gradients are employed for extended periods of time, even more so on

preclinical scanners. This decrease in signal intensity over time can cause mis-estimates of derived parameters and also affect tractography (218). While randomized diffusion gradient directions and b-values may alleviate this to some extent by randomizing directionality of this bias, this presence of signal drift can be examined, and corrected by collecting multiple  $b=0$  images throughout the scan to determine correction factors (typically linear or quadratic) to minimize this effect. Although this is not commonly done in the literature, we advocate for its use, and methodology and code to do so is described in (218) and in [Section 5.1.1](#).

#### 4.1.2 Cord & other organs

The spinal cord is part of the central nervous system. Its shape is similar to a cylinder of a few mm of diameter and several cm long (the size depends on the species and the age). Typically, diffusion imaging of the spinal cord focuses on its white matter which, conversely to the brain, is located at the periphery of the spinal cord (while the gray matter is inside and has a butterfly shape). Typical preprocessing steps for spinal cord include:

1. **Segmenting** the spinal cord (i.e. delineating the outer contour of the spinal cord) and the gray matter. This provides a mask of the white matter, which can then be used to extract diffusion metrics within the white matter. Spinal cord segmentation can be achieved using active contour (253), propagation of a 3D mesh (254) or deep learning (255). The two latter methods are available in the Spinal Cord Toolbox (SCT) (256). For more details on spinal cord segmentation, please see (257).
2. **Straightening** the spinal cord to have it aligned along the superior-inferior axis. The benefits of doing this step is to facilitate the registration to a spinal cord template and atlas, and/or for group analysis. Straightening the spinal cord can be done with SCT using an algorithm that preserves the topology of the internal structure of the spinal cord (258). This procedure outputs a forward and backward warping field that can be concatenated with the warping field used to register to a template (see below).
3. **Registering** the spinal cord to an anatomical template. This step is useful for extracting diffusion metrics within specific white matter tracts of the spinal cord, e.g., cortico-spinal, rubrospinal, dorsal columns. There exist a few spinal cord templates and atlases, for example the human *in vivo* PAM50 template (259), an *ex vivo* human template (260) and a rat spinal cord template (261).

An end-to-end analysis pipeline, with documentation, example data, and procedure for manual correction is available at <http://spine-generic.readthedocs.io/> (262). This project is for *in vivo* human spinal cord, but could be adapted for *ex vivo* and non-human species.

Diffusion MRI provides key information on microstructural properties not only in the central nervous system, but also in other organs such as liver (112), kidneys (263,264), prostate (265–267), muscle (268), heart (269), or even in the bone, as in the study of metastatic cancer (270,271). Imaging each of these anatomical districts *in vivo* comes with its own challenges, mainly related to complex motion patterns due to proximity to the lungs, inhomogeneous magnetic fields close to air cavities (e.g., stomach, lungs, rectum), pulsation effects, intrinsic low signal-to-noise ratio due to short  $T_2$  (e.g., in the liver, due to the presence of iron). Such challenges affect small animal imaging similarly as clinical imaging in humans. Typical pre-processing steps used for brain MRI can also be useful in these anatomical areas, e.g., denoising, motion and distortion correction, although at present there is still a lack of processing packages tailored for these applications. Another key difference as compared to central nervous system imaging is related to the different microstructural composition of these organs. Firstly, organs such as the liver or prostate are highly vascularised and feature strong intra-voxel incoherent motion (IVIM) effects. Secondly, cell sizes are much larger than in the brain (e.g., 20-40  $\mu\text{m}$  for hepatocytes (38,272)), implying that i) for the diffusion times used in brain imaging, intra-cellular diffusion signals may not still have reached long-time limits, ii) neglecting cell radius (i.e., using zero-radius approximations (273)) can lead to inaccurate intra-cellular signal representations. Thirdly, the anisotropy of the dMRI signal is typically much smaller than in the brain, so that directional schemes based on 3 mutually orthogonal diffusion directions can characterize tissue diffusion properties surprisingly well in some cases (274). Overall, this implies that biophysical dMRI models used for voxel-wise processing in the brain are not suited for application in abdominal/prostate/bone imaging, and alternative approaches tailored for the organs of interest need to be developed (265,274).

### 4.1.3 Where future work should lie

Non-human brain extraction is an important pre-processing step which, if inaccurate, can largely affect the performance of downstream steps. Preprocessing tools, at each step of the pipeline, should account for geometric and anatomical differences between species, and studies should be performed to optimize and standardize these tools depending on species. Finally, setting up a publicly available pipeline that integrates these pre-processing steps seamlessly, with optimized parameters for each species would be highly beneficial.

## 4.2 Processing pipelines

After pre-processing, it is typical to perform voxel-wise analysis of the diffusion-weighted measures to output parametric maps of a variety of derived metrics. These parametric maps can undergo subsequent analysis at the ROI, individual, or group-level.

Diffusion analyses typically used in human data can be applied to small-animal data: DTI, DKI, or a biophysical model suited for the tissue of interest (white matter, gray matter, muscle, prostate, various tumor types, etc.) (6,7,63,146,267). For DTI, many software tools are available - see [Section 5.1](#) for software and resources. Substantially fewer software packages also offer diffusion kurtosis estimation. It should be noted that most software do not check for  $b$ -value suitability prior to DTI or DKI estimation. We underline here that, to stay within the respective cumulant expansion regimes, the diffusion tensor *in vivo* should be estimated from  $b$ -values  $\leq 1000$  s/mm<sup>2</sup>, and diffusion and kurtosis tensors *in vivo* should be estimated jointly from at least two shells with  $b$ -values  $\leq 2500$  s/mm<sup>2</sup>. For biophysical model estimation, dedicated code is usually provided by the model developers.

Potential differences between human and small-animal diffusion analysis may stem from differences in brain anatomy and composition, as discussed in [Section 2.3](#): e.g., overwhelming gray matter and limited white matter in rodent brain, absence of gyrified cortex, myelination, cortical layer composition, bundle crossing/complexity.

Once parametric maps of various diffusion metrics are available in native space, it is common to use registration either to import atlas-based segmentation of brain regions for ROI analysis or to bring individual maps into a common space for voxel-based comparisons. For this registration/normalization step, typical tools used in human data also work well for animal data, with some customization. For non-linear registration for instance, default physical dimensions of warp and smoothing kernels should be scaled to those of small-animal brains.

Common MRI atlases, including brain segmentation, for a variety of species are provided in [Section 5.1.2](#).

### 4.2.1 Where future work should lie

Similar to preprocessing, free online sharing of processing tools can accelerate the harmonization process, and several efforts are already going in this direction (see also [Section 5.1.1](#) Code/Software). Moreover, prospective harmonization studies (275) are also required to understand and account for inter-site variability.

## 4.3 Tractography

The application and use of fiber tractography as a tool to study the fiber pathways and wiring diagram of the brain remain largely the same for small animals as for the *in vivo* human (192). In general, some measure of fiber orientation is estimated for each voxel, which is used to create continuous space curves (i.e., streamlines) which are thought of as representations of groups of axons traveling throughout the tissue. For these reasons, the fundamentals of tractography (deterministic and probabilistic algorithms) also remain the same, and guidelines follow those for human data. In our experience, the only required change is the brain masking approach, for which, as mentioned previously, there are very few brain-masking algorithms dedicated to small animals.

**Acquisition:** For tractography, we recommend acquiring data with isotropic resolution, as anisotropic voxel size can introduce bias in estimates of fractional anisotropy and hinder the ability of algorithms to deal with branching/bending pathways (276). Higher angular resolution and strong diffusion weightings are likely to benefit tractography, but need to be balanced with considerations for SNR and acquisition time. Typically, resolution is determined following the guidelines presented in [Section 3.7](#), and we recommend acquisitions having greater than 30 diffusion-weighted directions (and commonly 60-100+). While small animals, and *ex vivo* imaging in particular, enable high resolution scans, very high resolution does not always lead to improvements in tractography (132).

**Fiber Orientation Estimation:** Very few changes are needed in the voxel-wise reconstruction step. As described throughout this text, after acquisition and modeling have been adapted for animal imaging, all approaches to estimate fiber orientation distributions will work adequately in these model systems (including diffusion tensor imaging, spherical deconvolution, ball & sticks, and more advanced methods), resulting in a field of orientation estimates that can be used for tractography.

**Tractography:** Several changes are needed in the tractography process itself. For example, with smaller brains, smaller structures, and smaller voxel sizes, it is common that the “step size” in tractography algorithms must be reduced, although this will usually be performed by default in many software packages. The process of starting and stopping streamlines will also remain the same, with streamlines usually starting in the WM (or at the WM/GM interface) and propagating until it reaches the gray matter, or until the orientation becomes ambiguous (low FA, for example) or high curvature occurs. For this reason, most common software packages (MRtrix3, DSI Studio, DIPY, FSL, ExploreDTI) are able to easily be used for preclinical dMRI with

few modifications. Often, false positive streamlines are removed through filtering or clustering operations. If thresholding by streamline length, this threshold must be adapted to an appropriate measure for each specimen. In a human, common thresholds are to remove streamlines that are <20mm (to eliminate spurious streamlines) and >250mm (to remove implausibly long streamlines, or loops). The process of filtering by microstructural measures, or the diffusion signal (using algorithms such as LIFE (211), SIFT (209,210), or COMMIT (208)), as well as adding anatomical constraints, will also remain the same in animal models.

One application of tractography is for **bundle segmentation**. Individual fiber pathways, or fascicles, of the brain are virtually dissected to be studied across cohorts or across time. This is usually done by using regions of interest (ROIs) through which bundles must or must not pass through, to isolate a desired pathway. The most obvious change for animal models is that specific fiber pathways may or may not exist in the specimens under investigation, and if they do, they may not have a direct analogous cortical area that they connect or regions through which they must pass (277–279). Thus, ROIs must be modified in accordance with prior knowledge of the bundle. For this reason, many automated or manual protocols for bundle dissection are not readily adaptable for small animals. Although some works have described and created tools for dissection in some subjects (for example macaque (280), squirrel monkey (281), mouse (282), common tools and protocols for bundle segmentation in humans (283,284) have not yet been adapted. Modifying these tools for different model systems will involve defining atlases, regions, or template streamlines, which should prove useful to the field. Regarding the analysis of bundles, quantifying microstructure along or within the bundle of interest (285) (286)) connectivity and shape of the bundles (287) can be done using the same analysis as for human data.

The next common application of tractography is **connectome analysis** - an analysis of the set of streamlines throughout the entire brain to determine network properties, often using graph-theoretic measures. Connectome analysis remains largely unchanged in preclinical data, as well as the quantification and analysis of connectivity matrices and graph measures. Potential differences in connectome analysis include different edges/nodes used to derive the matrix, which will typically be derived from existing templates and atlases (281,288–291).

To summarize guidelines for tractography: Follow the tractography process in the same way as for *in vivo* human data, but adopt choices and parameters based on the system being studied. Regions for bundle segmentation must be justified by a priori knowledge of the studied pathway. To date, comparisons of histology and tractography in animal systems serve as gold standards for validation studies, and are responsible for a majority of our knowledge of the

limitations and successes of the tractography process. Thus, tractography performed in the animal generally follows the same results, logic, and decisions that would be done in human data.

### 4.3.1 Where future work should lie

As described above, while the process of tractography in the animal strongly parallels that of the human, there are still areas for which no guidelines can be provided. In humans, researchers have slowly settled upon acquiring images with isotropic acquisition, with 2-mm isotropic resolution becoming largely clinically feasible in short scan times; it is unknown what resolution is necessary in various animal brains. Many *in vivo* animal studies still rely on anisotropic slices, which can introduce biases in anisotropy measures and tractography (292).

For the tractography process, it is unclear if specific modifications to the generation of streamlines are needed. For example, it may be necessary to adopt starting/stopping criteria, curvature thresholds, or anisotropy criteria for animals with different GM/WM volumes, different (both more or less complex) geometries, and different expected curvatures or pathways. It is also unclear how many streamlines are needed for whole brain tractography to capture most axonal pathways for connectome analysis. Additionally, with the benefits of preclinical magnets and high-gradients comes the ability to image, and possibly probe connections within cortical or deep gray matter areas, an area that is relatively unexplored in the human brain, and for which there are little-to-no known guidelines.

Also, few guidelines are provided on optimal regions and region placement for bundle segmentation. Many human protocols and algorithms rely on regions located in a standard space (typically MNI 152), that have been modified and tailored over the years to continually improve the resulting tractography dissections. Very few studies exist which describe appropriate region placement in animal models.

Rather than debate or controversy, most of the lack of guidelines comes from a sparsity of resources dedicated to tractography in the animal models. Thus, we propose that future work should lie in creating resources that allow whole brain tractography (possibly informed by anatomical constraints) in various models, followed by atlas-based labeling (to create nodes/edges for connectome generation), and bundle dissection for pathways of interest. This, of course, relies on the creation of appropriate templates and atlases (of which several exist for many species), and also the prior knowledge of the existence, or lack thereof, of certain bundles in each species. The creation of manual protocols, standard regions, or even streamline-based atlases, will allow automated bundle dissection methods to study changes and differences in

pathways reliably and reproducibly. Of particular interest to comparative anatomists would be a way to compare individuals or groups of bundles across species.

As described above, one necessary component of many pipelines is brain masking and white matter/gray matter segmentation, to act as streamline start/end points and facilitate anatomical constraints in tractography. There are remarkably few tools available to do this in animal models, in contrast to the multitude of skull-stripping and segmentation tools in the human literature. Species-specific masking and tissue-segmentation would be useful for tractography, and animal research in general, and should be pursued in the future, possibly utilizing shape priors, or priors on the diffusion signal itself (110,192).

In regards to validation, tractography is often validated on the animal models, with the knowledge that the process itself is strongly similar (and thus shares similar limitations) as that in the human. Thus, we should strive to understand and quantify differences between tractography and tracer, and relate these to situations that may occur in the human brain. For example, knowledge of complications due to crossing fibers (293), due to spatial resolution (294,295), bottle-neck regions of tractography (131,296,297), superficial U-fibers (298), effects of experimental parameters (299), and false-positives and false-negatives (138) have been elucidated through the use of animal models - and we should continually understand the parallels to the human brain to reliably interpret measures derived from tractography.

## 5 Perspectives

### 5.1 Open science

#### 5.1.1 Code/Software

Challenges with pre-processing and processing pipelines highlighted in the previous sections could start to be overcome through code sharing and harmonization of implementations. Sharing combined knowledge and experience of many groups is valuable as it generates a lower barrier to entry and an excellent opportunity to evaluate robustness and reproducibility.

In order to allow for a more dynamic and self-updating resource center, and facilitate code sharing, we have compiled a (non-comprehensive) list of available software dedicated to the acquisition and processing of preclinical dMRI data, meant to be updated regularly, on a public repository: <https://github.com/Diffusion-MRI/awesome-preclinical-diffusion-mri.git>.

Updates on available software and tools can be shared by developers and users can ask questions/advice for implementation, etc.

## 5.1.2 Data Sharing & Databases

A critical aspect of data sharing is making sure one dataset can easily be reused by others. The F.A.I.R. principles (300), stating that data should be findable, accessible, interoperable, and reusable, provide general principles for how data and metadata should be organized and detailed that now are widely accepted by researchers and funding agencies. Several practical solutions and implementations for FAIR sharing of image data have emerged, including EBRAINS (<http://ebrains.eu/>).

Standards for naming and organizing folders and files are of key importance for the reusability of shared imaging data. The neuroimaging community therefore came up with the Brain Imaging Data Structure (BIDS) (301), recently endorsed as a standard by the International Neuroinformatics Coordinating Facility (INCF) (302). In brief, data are organized according to contrasts (*anat*, *dwi*). File names include relevant suffix that help researchers and software figure out the origin and intention of the files (e.g., “\_dwi” is intended for diffusion weighted analysis). Sidecar JSON files include additional metadata that are relevant for the analysis. **Figure 6** illustrates a dataset structured according to BIDS. While the BIDS standard has originally been motivated by the brain functional MRI community, this standard is being actively expanded to accommodate more MR techniques and modalities (e.g. MEG, EEG) via its BIDS extension proposals<sup>1</sup>, the latest of which also include advanced diffusion-weighted imaging (303). Also relevant are BIDS standards for microscopy data (304) and recent initiatives for incorporating animal data into the BIDS standard (<https://bids.neuroimaging.io/bep032>).

---

<sup>1</sup> [https://bids.neuroimaging.io/get\\_involved.html#extending-the-bids-specification](https://bids.neuroimaging.io/get_involved.html#extending-the-bids-specification)

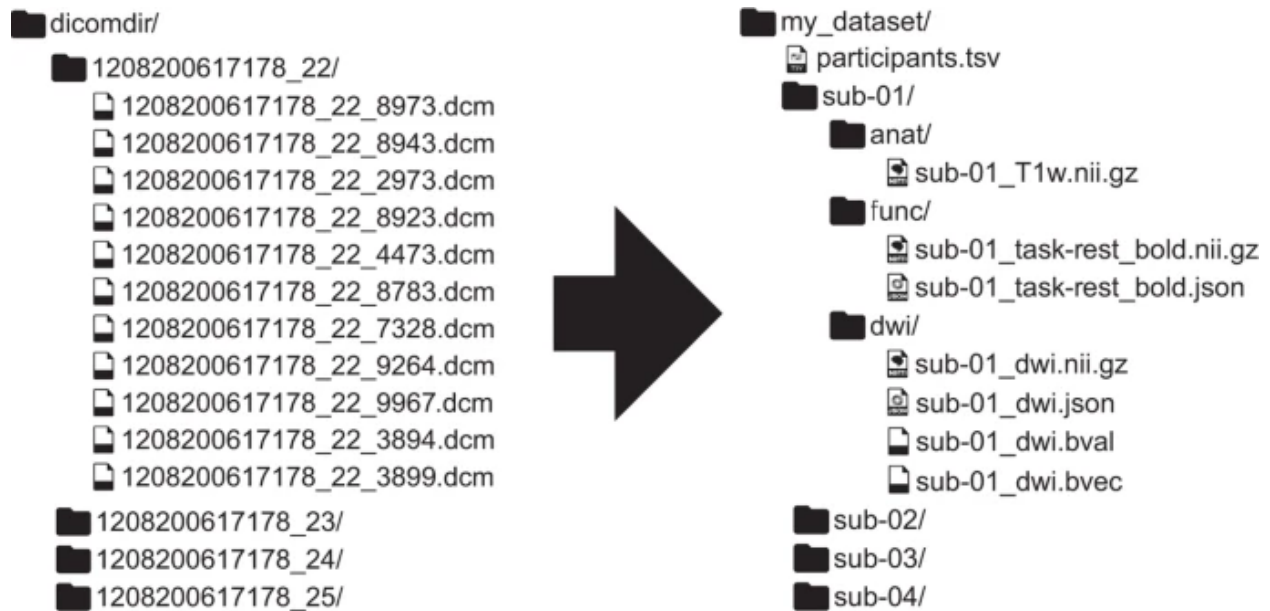


**Figure 6.** Illustration of a BIDS structured dataset. From (301)

In addition to facilitating data sharing, data organization standards like BIDS help designing applications that know *where* to look for input data. This ultimately helps automating analysis tasks and creating pipelines. A list of BIDS-compatible apps is available at <https://bids-apps.neuroimaging.io/apps/>.

Platforms that could serve as a repository for pre-clinical datasets include OSF, OpenNeuro, Zenodo, NITRC, or other center resources (e.g. US National High Magnetic Field Laboratory).

To promote data sharing and reuse, we compiled a (non-comprehensive) list of existing freely shared small-animal or *ex vivo* diffusion-weighted datasets, available on a public repository: <https://github.com/Diffusion-MRI/awesome-preclinical-diffusion-mri.git>. As for code sharing, the repository will enable a regular update of this database by the community.

### 5.1.3 Where future work should lie

Code can be hosted on platforms such as GitHub, GitLab, Zenodo, NITRC etc. Hosting code via these tools is not only beneficial for the community, but also for the code developers themselves (and their respective research groups). Indeed, this ensures code safekeeping, retrieving and versioning. Nevertheless, code sharing platforms are not scratchpads for any code. Sharing code also comes with the responsibilities of documenting, cleaning, packaging, testing and versioning the code. These duties come at a (high) cost of requiring an in situ software

engineer. Initiatives aimed at allocating special resources for software maintenance via funding bodies would be much welcome.

In terms of licensing open source code, there exist different options. Some of the most permissive licenses include MIT and BSD licenses. It means that the code can be reused by any entity (person or company), and importantly to note, is that the modified code can be distributed as closed source. If you wish to enforce the disclosure of your open source code, there are so-called 'copyleft' licenses, such as the GNU GPLv3 and the Mozilla Public License 2.0. For more details, see <https://choosealicense.com/licenses/>.

Certainly one of the highest aims is to propose a successful, transparent and comprehensive analysis framework that promotes reproducibility.

The amount of open-source code and data is overwhelming. Sharing code and data is a double edged sword. Indeed, public sharing of scientific objects that do not meet certain standards or requirements can do more harm than good.

Let us take the example of a paper, for which the underlying data and analysis script are shared on OSF. On the one hand, the uploaded script may not be foolproof, and its subsequent fixes not updated on OSF. One solution to this issue is to keep code on a dedicated platform (e.g. GitHub) and pointing to a specific tag or commit hashtag directly in the associated paper and OSF data repository. On the other hand, the originally shared data on OSF may be updated with additional subjects, but the original paper does not specify the version of the dataset that it uses. One solution to this is to version-track the dataset itself and mention its version in the paper.

Several software solutions exist to link data objects and code and track provenance, for example Datalad (<https://www.datalad.org/>) and the YODA framework (<https://handbook.datalad.org/en/latest/basics/101-127-yoda.html>).

## 5.2 The future: what should we strive to achieve?

As a field, we should continually strive to achieve reduced barriers to entry for new imaging centers, new scientists, and new industries who aim to use dMRI in a preclinical setting. Towards this end, as a community, we should promote dissemination of knowledge, code, and datasets to achieve high standards of data quality and analysis, reproducibility, transparency and foster collaborations, as well as reduce globally the time and cost of research in this field.

From a **hardware** perspective, ever stronger magnets and gradients, ever faster slew rates will keep pushing the capabilities of the field forward. Progress in multi-channel coil designs for preclinical imaging would be extremely valuable not only for reducing scan time using

GRAPPA-like acceleration methods and/or simultaneous multislice (SMS) excitations but also for reducing artifacts.

In the interest of improved reproducibility and cross-site comparisons, systematic reporting of animal **physiology** (at the very least respiration rate and core temperature) and **anesthesia** procedures in dMRI publications is highly encouraged.

As far as **diffusion acquisition** is concerned, the flexibility associated with preclinical MRI scanners will hopefully foster further developments in terms of novel diffusion encoding and acquisition techniques to bring dMRI ever closer to *in vivo* histology. On a more practical level, the randomized order of acquisition for different  $b$ -values and diffusion times, along with interspersed  $b=0$  images to control for drifts, temperature changes and/or physiological effects should be increasingly adopted; this effort would be greatly supported by enabling this option in vendor default sequences, as opposed to users creating and loading custom files with such a random design. The harmonization of acquisition protocols (e.g. as to the choice of  $b_{\max} = 1000$  s/mm<sup>2</sup> for DTI and  $b_{\max} = 2500$  s/mm<sup>2</sup> for DKI *in vivo*) may help multi-site reproducibility and comparison studies. Notwithstanding, encouraging the community to acquire richer datasets by default (e.g. multi-shell at minimum, but even for multiple diffusion times) can open up many avenues for testing new models retrospectively on public datasets, in a variety of animal models, healthy and diseased. Within such rich datasets, it is recommended to adopt a consistent echo time for all diffusion-weighted images, since accounting for variable  $T_2$ -weighting considerably complicates the data analysis.

**Pre-processing** steps are far from being optimized and integrated into a seamless pipeline for small animal dMRI, so an initiative in this direction, ideally for each species, would highly benefit the community. Brain extraction in particular seems to deserve dedicated attention and impacts the quality of downstream pre-processing steps substantially.

Transparent **processing** pipelines should also become the norm in the near future, though given the diversity and complexity of possible dMRI analyses, harmonization may be out of reach or even unjustified. We encourage new community members to search for existing tools in our GitHub database and expand/build on that.

New **biophysical models** of tissue are typically initially tested in a preclinical imaging setting. We underline that the development of new models should uphold high standards in terms of accuracy and precision of microstructural features estimated, and be validated using complementary techniques such as light or electron microscopy.

Rather than debate or controversy, most of the lack of **tractography** guidelines comes from a sparsity of resources dedicated to this application in the animal models. Future work could

thus lie in creating resources that allow whole brain tractography in various species, followed by atlas-based labeling and bundle dissection for pathways of interest. As for biophysical models of microstructure, tractography is often validated in a preclinical setting. Thus, another path for future efforts is to understand and quantify differences between tractography and tracer, and to relate these to situations that may occur in the human brain.

To remain consistent with  $b$ -value units of  $\text{s/mm}^2$  typically set at the scanner console and with “common language”, we have reported  $b$ -values in  $\text{s/mm}^2$  and diffusivities in  $\text{mm}^2/\text{s}$  throughout this work. However, we would like to encourage the community to gradually adopt units that are more suitable for dMRI of biological tissue, where diffusion lengths are on the order of a few microns and diffusion times on the order of a few ms. Hence diffusivities expressed in  $\mu\text{m}^2/\text{ms}$  and  $b$ -values expressed in  $\text{ms}/\mu\text{m}^2$  are much more “natural” and enable to juggle numbers close to unity vs thousands (e.g.  $b=1 \text{ ms}/\mu\text{m}^2$  vs  $b=1000 \text{ s/mm}^2$ ) or decimals (e.g.  $D=1 \mu\text{m}^2/\text{ms}$  vs  $D=10^{-3} \text{ mm}^2/\text{s}$ ). Some of the recent literature on dMRI microstructure models have adopted this new convention, and we hope it will prevail in the near future.

**Open science:** One of the main challenges and goals for the preclinical dMRI community is to responsibly share code and data, and develop transparent and comprehensive analysis frameworks that promote reproducibility. In order to provide a useful resource and starting point, we have created a dedicated github repository where publicly available datasets, software and tools are collected, and which will be updated regularly.

## 6 Acknowledgements and Support

The authors acknowledge financial support from: the National Institutes of Health (K01EB032898, R01AG057991, R01NS125020, R01EB017230, R01EB019980, R01EB031954, R01CA160620, R01NS109090), the National Institute of Biomedical Imaging and Bioengineering (R01EB031765, R56EB031765), the National Institute on Drug Abuse (P30DA048742), the Secretary of Universities and Research (Government of Catalonia) Beatriu de Pinós postdoctoral fellowship (2020 BP 00117), “la Caixa” Foundation Junior Leader fellowship (LCF/BQ/PR22/11920010), the Research Foundation Flanders (FWO: 12M3119N), the Belgian Science Policy Prodex (Grant ISLRA 2009–1062), the  $\mu$ NEURO Research Center of Excellence of the University of Antwerp, the Institutional research chair in Neuroinformatics (Sherbrooke, Canada), the NSERC Discovery Grant, the European Research Council Consolidator grant (101044180), the Canada Research Chair in Quantitative Magnetic Resonance Imaging [950-230815], the Canadian Institute of Health Research [CIHR FDN-143263], the Canada Foundation for Innovation [32454, 34824], the Fonds de Recherche du Québec - Santé [322736], the Natural Sciences and Engineering Research

Council of Canada [RGPIN-2019-07244], the Canada First Research Excellence Fund (IVADO and TransMedTech), the Courtois NeuroMod project, the Quebec BioImaging Network [5886, 35450], the Mila - Tech Transfer Funding Program, the Swiss National Science Foundation (Eccellenza Fellowship PCEFP2\_194260), the Swiss State Secretariat for Education, Research and Innovation (MB22.00032) and the CIBM Center for Biomedical Imaging, Switzerland.

## 7 References

1. Moseley ME, Kucharczyk J, Mintorovitch J, et al. Diffusion-weighted MR imaging of acute stroke: correlation with T2-weighted and magnetic susceptibility-enhanced MR imaging in cats. *AJNR Am. J. Neuroradiol.* 1990;11:423–429.
2. Basser PJ, Mattiello J, LeBihan D. MR diffusion tensor spectroscopy and imaging. *Biophysical Journal* 1994;66:259–267 doi: 10.1016/s0006-3495(94)80775-1.
3. Jones DK. *Diffusion MRI: Theory, Methods, and Application.*; 2010.
4. Moseley ME, Cohen Y, Kucharczyk J, et al. Diffusion-weighted MR imaging of anisotropic water diffusion in cat central nervous system. *Radiology* 1990;176:439–445.
5. Dyrby TB, Innocenti GM, Bech M, Lundell H. Validation strategies for the interpretation of microstructure imaging using diffusion MRI. *Neuroimage* 2018;182:62–79.
6. Jelescu IO, Budde MD. Design and validation of diffusion MRI models of white matter. *Front. Phys.* 2017;28 doi: 10.3389/fphy.2017.00061.
7. Jelescu IO, Palombo M, Bagnato F, Schilling KG. Challenges for biophysical modeling of microstructure. *J. Neurosci. Methods* 2020;344:108861.
8. Barazany D, Basser PJ, Assaf Y. In vivo measurement of axon diameter distribution in the corpus callosum of rat brain. *Brain* 2009;132:1210–1220.
9. Iima M, Reynaud O, Tsurugizawa T, et al. Characterization of glioma microcirculation and tissue features using intravoxel incoherent motion magnetic resonance imaging in a rat brain model. *Invest. Radiol.* 2014;49:485–490.
10. Caruyer E, Lenglet C, Sapiro G, Deriche R. Design of multishell sampling schemes with uniform coverage in diffusion MRI. *Magn. Reson. Med.* 2013;69:1534–1540.
11. Szczepankiewicz F, Westin C-F, Nilsson M. Gradient waveform design for tensor-valued encoding in diffusion MRI. *J. Neurosci. Methods* 2021;348:109007.
12. Wu D, Xu J, McMahon MT, et al. In vivo high-resolution diffusion tensor imaging of the mouse brain. *Neuroimage* 2013;83:18–26.
13. Grier MD, Yacoub E, Adriany G, et al. Ultra-high field (10.5T) diffusion-weighted MRI of the macaque brain. *Neuroimage* 2022;255:119200.
14. Jelescu IO, Zurek M, Winters KV, et al. In vivo quantification of demyelination and recovery using compartment-specific diffusion MRI metrics validated by electron microscopy. *Neuroimage* 2016;132:104–114.
15. Mishra A, Wang F, Chen LM, Gore JC. Longitudinal changes in DTI parameters of specific spinal white matter tracts correlate with behavior following spinal cord injury in monkeys. *Sci. Rep.* 2020;10:17316.
16. Takemura H, Pestilli F, Weiner KS. Comparative neuroanatomy: Integrating classic and modern methods to understand association fibers connecting dorsal and ventral visual cortex. *Neurosci. Res.* 2019;146:1–12.
17. Budinger TF, Bird MD, Frydman L, et al. Toward 20 T magnetic resonance for human brain studies: opportunities for discovery and neuroscience rationale. *Magnetic Resonance Materials in Physics, Biology and Medicine* 2016;29:617–639 doi: 10.1007/s10334-016-0561-4.
18. van Bentum PJM, Janssen JWG, Kentgens APM. Towards nuclear magnetic resonance micro-spectroscopy and micro-imaging. *Analyst* 2004;129:793–803.

19. Does MD, Parsons EC, Gore JC. Oscillating gradient measurements of water diffusion in normal and globally ischemic rat brain. *Magn. Reson. Med.* 2003;49:206–215.
20. Aggarwal M, Smith MD, Calabresi PA. Diffusion-time dependence of diffusional kurtosis in the mouse brain. *Magn. Reson. Med.* 2020;84:1564–1578.
21. Pyatigorskaya N, Le Bihan D, Reynaud O, Ciobanu L. Relationship between the diffusion time and the diffusion MRI signal observed at 17.2 Tesla in the healthy rat brain cortex. *Magn. Reson. Med.* 2014;72:492–500.
22. Wu D, Martin LJ, Northington FJ, Zhang J. Oscillating gradient diffusion MRI reveals unique microstructural information in normal and hypoxia-ischemia injured mouse brains. *Magn. Reson. Med.* 2014;72:1366–1374.
23. Jespersen SN, Bjarkam CR, Nyengaard JR, et al. Neurite density from magnetic resonance diffusion measurements at ultrahigh field: comparison with light microscopy and electron microscopy. *Neuroimage* 2010;49:205–216.
24. Seppehrband F, Alexander DC, Kurniawan ND, Reutens DC, Yang Z. Towards higher sensitivity and stability of axon diameter estimation with diffusion-weighted MRI. *NMR Biomed.* 2016;29:293–308.
25. Xu J, Li H, Harkins KD, et al. Mapping mean axon diameter and axonal volume fraction by MRI using temporal diffusion spectroscopy. *Neuroimage* 2014;103:10–19.
26. İanuş A, Jespersen SN, Serradas Duarte T, Alexander DC, Drobnjak I, Shemesh N. Accurate estimation of microscopic diffusion anisotropy and its time dependence in the mouse brain. *Neuroimage* 2018;183:934–949.
27. Lundell H, Nilsson M, Dyrby TB, et al. Multidimensional diffusion MRI with spectrally modulated gradients reveals unprecedented microstructural detail. *Sci. Rep.* 2019;9:9026.
28. Jirjis MB, Valdez C, Vedantam A, Schmit BD, Kurpad SN. Diffusion tensor imaging as a biomarker for assessing neuronal stem cell treatments affecting areas distal to the site of spinal cord injury. *J. Neurosurg. Spine* 2017;26:243–251.
29. Otero-Ortega L, Gutiérrez-Fernández M, Ramos-Cejudo J, et al. White matter injury restoration after stem cell administration in subcortical ischemic stroke. *Stem Cell Res. Ther.* 2015;6:121.
30. Rasmussen AL, Okumura A, Ferris MT, et al. Host genetic diversity enables Ebola hemorrhagic fever pathogenesis and resistance. *Science* 2014;346:987–991.
31. Liovat A-S, Jacquelin B, Ploquin MJ, Barré-Sinoussi F, Müller-Trutwin MC. African non human primates infected by SIV - why don't they get sick? Lessons from studies on the early phase of non-pathogenic SIV infection. *Curr. HIV Res.* 2009;7:39–50.
32. Hutchison RM, Womelsdorf T, Gati JS, Everling S, Menon RS. Resting-state networks show dynamic functional connectivity in awake humans and anesthetized macaques. *Hum. Brain Mapp.* 2013;34:2154–2177.
33. Assaf Y, Bouznach A, Zomet O, Marom A, Yovel Y. Conservation of brain connectivity and wiring across the mammalian class. *Nat. Neurosci.* 2020;23:805–808.
34. Wang SS-H, S.-H. Wang S, Shultz JR, et al. Functional Trade-Offs in White Matter Axonal Scaling. *Journal of Neuroscience* 2008;28:4047–4056 doi: 10.1523/jneurosci.5559-05.2008.
35. Caminiti R, Ghaziri H, Galuske R, Hof PR, Innocenti GM. Evolution amplified processing with temporally dispersed slow neuronal connectivity in primates. *Proc. Natl. Acad. Sci. U. S. A.* 2009;106:19551–19556.
36. Mota B, Dos Santos SE, Ventura-Antunes L, et al. White matter volume and white/gray matter

ratio in mammalian species as a consequence of the universal scaling of cortical folding. *Proc. Natl. Acad. Sci. U. S. A.* 2019;116:15253–15261.

37. Imamura H, Kawasaki S, Shiga J, Bandai Y, Sanjo K, Idezuki Y. Quantitative evaluation of parenchymal liver cell volume and total hepatocyte number in cirrhotic patients. *Hepatology* 1991;14:448–453.

38. Martin NC, McCullough CT, Bush PG, Sharp L, Hall AC, Harrison DJ. Functional analysis of mouse hepatocytes differing in DNA content: volume, receptor expression, and effect of IFN $\gamma$ . *J. Cell. Physiol.* 2002;191:138–144.

39. Abu Toamih Atamni H, Nashef A, Iraqi FA. The Collaborative Cross mouse model for dissecting genetic susceptibility to infectious diseases. *Mamm. Genome* 2018;29:471–487.

40. Becker AJ. Review: Animal models of acquired epilepsy: insights into mechanisms of human epileptogenesis. *Neuropathology and Applied Neurobiology* 2018;44:112–129 doi: 10.1111/nan.12451.

41. Hajiaghamemar M, Seidi M, Oeur RA, Margulies SS. Toward development of clinically translatable diagnostic and prognostic metrics of traumatic brain injury using animal models: A review and a look forward. *Exp. Neurol.* 2019;318:101–123.

42. Rumpel H, Nedelcu J, Aguzzi A, Martin E. Late glial swelling after acute cerebral hypoxia-ischemia in the neonatal rat: a combined magnetic resonance and histochemical study. *Pediatr. Res.* 1997;42:54–59.

43. Wu D, Martin LJ, Northington FJ, Zhang J. Oscillating-gradient diffusion magnetic resonance imaging detects acute subcellular structural changes in the mouse forebrain after neonatal hypoxia-ischemia. *J. Cereb. Blood Flow Metab.* 2019;39:1336–1348.

44. Guglielmetti C, Veraart J, Roelant E, et al. Diffusion kurtosis imaging probes cortical alterations and white matter pathology following cuprizone induced demyelination and spontaneous remyelination. *Neuroimage* 2016;125:363–377.

45. Kelm ND, West KL, Carson RP, Gochberg DF, Ess KC, Does MD. Evaluation of diffusion kurtosis imaging in ex vivo hypomyelinated mouse brains. *Neuroimage* 2016;124:612–626.

46. Chuhutin A, Hansen B, Wlodarczyk A, Owens T, Shemesh N, Jespersen SN. Diffusion Kurtosis Imaging maps neural damage in the EAE model of multiple sclerosis. *Neuroimage* 2020;208:116406.

47. Wu Q-Z, Yang Q, Cate HS, et al. MRI identification of the rostral-caudal pattern of pathology within the corpus callosum in the cuprizone mouse model. *J. Magn. Reson. Imaging* 2008;27:446–453.

48. Xie M, Tobin JE, Budde MD, et al. Rostrocaudal analysis of corpus callosum demyelination and axon damage across disease stages refines diffusion tensor imaging correlations with pathological features. *J. Neuropathol. Exp. Neurol.* 2010;69:704–716.

49. Laitinen T, Sierra A, Pitkänen A, Gröhn O. Diffusion tensor MRI of axonal plasticity in the rat hippocampus. *NeuroImage* 2010;51:521–530 doi: 10.1016/j.neuroimage.2010.02.077.

50. Kharatishvili I, Immonen R, Gröhn O, Pitkänen A. Quantitative diffusion MRI of hippocampus as a surrogate marker for post-traumatic epileptogenesis. *Brain* 2007;130:3155–3168.

51. Sierra A, Laitinen T, Gröhn O, Pitkänen A. Diffusion tensor imaging of hippocampal network plasticity. *Brain Struct. Funct.* 2015;220:781–801.

52. Mac Donald CL, Dikranian K, Bayly P, Holtzman D, Brody D. Diffusion tensor imaging reliably detects experimental traumatic axonal injury and indicates approximate time of injury. *J. Neurosci.* 2007;27:11869–11876.

53. Hutchinson EB, Schwerin SC, Radomski KL, et al. Detection and Distinction of Mild Brain Injury Effects in a Ferret Model Using Diffusion Tensor MRI (DTI) and DTI-Driven Tensor-Based Morphometry (D-TBM). *Front. Neurosci.* 2018;12:573.
54. Wallace EJ, Mathias JL, Ward L. Diffusion tensor imaging changes following mild, moderate and severe adult traumatic brain injury: a meta-analysis. *Brain Imaging Behav.* 2018;12:1607–1621.
55. Eierud C, Craddock RC, Fletcher S, et al. Neuroimaging after mild traumatic brain injury: review and meta-analysis. *Neuroimage Clin* 2014;4:283–294.
56. Chenevert TL, Stegman LD, Taylor JM, et al. Diffusion magnetic resonance imaging: an early surrogate marker of therapeutic efficacy in brain tumors. *J. Natl. Cancer Inst.* 2000;92:2029–2036.
57. Hamstra DA, Lee KC, Moffat BA, Chenevert TL, Rehemtulla A, Ross BD. Diffusion magnetic resonance imaging: an imaging treatment response biomarker to chemoradiotherapy in a mouse model of squamous cell cancer of the head and neck. *Transl. Oncol.* 2008;1:187–194.
58. Moffat BA, Hall DE, Stojanovska J, et al. Diffusion imaging for evaluation of tumor therapies in preclinical animal models. *MAGMA* 2004;17:249–259.
59. Kim S, Decarlo L, Cho GY, et al. Interstitial fluid pressure correlates with intravoxel incoherent motion imaging metrics in a mouse mammary carcinoma model. *NMR Biomed.* 2012;25:787–794.
60. Lesbats C, Kelly CL, Czanner G, Poptani H. Diffusion kurtosis imaging for characterizing tumor heterogeneity in an intracranial rat glioblastoma model. *NMR Biomed.* 2020;33:e4386.
61. de Jong M, Maina T. Of mice and humans: are they the same?--Implications in cancer translational research. *J. Nucl. Med.* 2010;51:501–504.
62. Jiang X, Li H, Xie J, Zhao P, Gore JC, Xu J. Quantification of cell size using temporal diffusion spectroscopy. *Magn. Reson. Med.* 2016;75:1076–1085.
63. Reynaud O. Time-dependent diffusion MRI in cancer: tissue modeling and applications. *Frontiers in Physics* 2017.
64. Reynaud O, Winters KV, Hoang DM, Wadghiri YZ, Novikov DS, Kim SG. Surface-to-volume ratio mapping of tumor microstructure using oscillating gradient diffusion weighted imaging. *Magn. Reson. Med.* 2016;76:237–247.
65. Zhang L, Yang L-Q, Wen L, et al. Noninvasively Evaluating the Grading of Glioma by Multiparametric Magnetic Resonance Imaging. *Acad. Radiol.* 2021;28:e137–e146.
66. Colvin DC, Yankeelov TE, Does MD, Yue Z, Quarles C, Gore JC. New insights into tumor microstructure using temporal diffusion spectroscopy. *Cancer Res.* 2008;68:5941–5947.
67. van de Looij Y, Vasung L, Sizonenko SV, Hüppi PS. MRI of animal models of developmental disorders and translation to human imaging. *Curr. Opin. Neurol.* 2014;27:157–167.
68. Hammelrath L, Škokić S, Khmelinskii A, et al. Morphological maturation of the mouse brain: An in vivo MRI and histology investigation. *Neuroimage* 2016;125:144–152.
69. Wu D, Zhang J. Recent Progress in Magnetic Resonance Imaging of the Embryonic and Neonatal Mouse Brain. *Front. Neuroanat.* 2016;10:18.
70. Alomair OI, Brereton IM, Smith MT, Galloway GJ, Kurniawan ND. In vivo high angular resolution diffusion-weighted imaging of mouse brain at 16.4 Tesla. *PLoS One* 2015;10:e0130133.
71. Yon M, Bao Q, Chitrit OJ, Henriques RN, Shemesh N, Frydman L. High-Resolution 3D in vivo Brain Diffusion Tensor Imaging at Ultrahigh Fields: Following Maturation on Juvenile and Adult Mice. *Front. Neurosci.* 2020;14:590900.
72. Badea A, Ng KL, Anderson RJ, Zhang J, Miller MI, O'Brien RJ. Magnetic resonance imaging

- of mouse brain networks plasticity following motor learning. *PLoS One* 2019;14:e0216596.
73. Mori S, Itoh R, Zhang J, et al. Diffusion tensor imaging of the developing mouse brain. *Magn. Reson. Med.* 2001;46:18–23.
74. Dall’Ara E, Boudiffa M, Taylor C, et al. Longitudinal imaging of the ageing mouse. *Mech. Ageing Dev.* 2016;160:93–116.
75. Song X, García-Saldivar P, Kindred N, et al. Strengths and challenges of longitudinal non-human primate neuroimaging. *Neuroimage* 2021;236:118009.
76. Liu Z, Wang X, Newman N, Grant KA, Studholme C, Kroenke CD. Anatomical and diffusion MRI brain atlases of the fetal rhesus macaque brain at 85, 110 and 135 days gestation. *Neuroimage* 2020;206:116310.
77. Wang X, Studholme C, Grigsby PL, Frias AE, Cuzon Carlson VC, Kroenke CD. Folding, But Not Surface Area Expansion, Is Associated with Cellular Morphological Maturation in the Fetal Cerebral Cortex. *J. Neurosci.* 2017;37:1971–1983.
78. Roberts VHJ, Lo JO, Lewandowski KS, et al. Adverse Placental Perfusion and Pregnancy Outcomes in a New Nonhuman Primate Model of Gestational Protein Restriction. *Reprod. Sci.* 2018;25:110–119.
79. Song S-K, Kim JH, Lin S-J, Brendza RP, Holtzman DM. Diffusion tensor imaging detects age-dependent white matter changes in a transgenic mouse model with amyloid deposition. *Neurobiol. Dis.* 2004;15:640–647.
80. Anckaerts C, Blockx I, Summer P, et al. Early functional connectivity deficits and progressive microstructural alterations in the TgF344-AD rat model of Alzheimer’s Disease: A longitudinal MRI study. *Neurobiol. Dis.* 2019;124:93–107.
81. Tristão Pereira C, Diao Y, Yin T, et al. Synchronous nonmonotonic changes in functional connectivity and white matter integrity in a rat model of sporadic Alzheimer’s disease. *Neuroimage* 2021;225:117498.
82. Steventon JJ, Trueman RC, Ma D, et al. Longitudinal in vivo MRI in a Huntington’s disease mouse model: Global atrophy in the absence of white matter microstructural damage. *Sci. Rep.* 2016;6:1–12.
83. Oguz I, McMurray MS, Styner M, Johns JM. The translational role of diffusion tensor image analysis in animal models of developmental pathologies. *Dev. Neurosci.* 2012;34:5–19.
84. Müller H-P, Roselli F, Rasche V, Kassubek J. Diffusion Tensor Imaging-Based Studies at the Group-Level Applied to Animal Models of Neurodegenerative Diseases. *Front. Neurosci.* 2020;14:734.
85. Pletnikov MV, Ayhan Y, Nikolskaia O, et al. Inducible expression of mutant human DISC1 in mice is associated with brain and behavioral abnormalities reminiscent of schizophrenia. *Mol. Psychiatry* 2008;13:173–86, 115.
86. Semple BD, Carlson J, Noble-Haeusslein LJ. Pediatric Rodent Models of Traumatic Brain Injury. *Methods Mol. Biol.* 2016;1462:325–343.
87. Mikkelsen SH, Wied B, Dashkovskiy V, et al. Head holder and cranial window design for sequential magnetic resonance imaging and optical imaging in awake mice. *Front. Neurosci.* 2022;16:926828.
88. De Groof G, Van der Linden A. Love songs, bird brains and diffusion tensor imaging. *NMR Biomed.* 2010;23:873–883.
89. Aggarwal M, Mori S, Shimogori T, Blackshaw S, Zhang J. Three-dimensional diffusion tensor microimaging for anatomical characterization of the mouse brain. *Magn. Reson. Med.*

2010;64:249–261.

90. Harsan L-A, Paul D, Schnell S, et al. In vivo diffusion tensor magnetic resonance imaging and fiber tracking of the mouse brain. *NMR Biomed.* 2010;23:884–896.
91. Nouls JC, Badea A, Anderson RBJ, Cofer GP, Allan Johnson G. Diffusion tensor imaging using multiple coils for mouse brain connectomics. *NMR Biomed.* 2018;31:e3921.
92. Calabrese E, Badea A, Cofer G, Qi Y, Johnson GA. A Diffusion MRI Tractography Connectome of the Mouse Brain and Comparison with Neuronal Tracer Data. *Cereb. Cortex* 2015;25:4628–4637.
93. Gyengesi E, Calabrese E, Sherrier MC, Johnson GA, Paxinos G, Watson C. Semi-automated 3D segmentation of major tracts in the rat brain: comparing DTI with standard histological methods. *Brain Struct. Funct.* 2014;219:539–550.
94. Figini M, Zucca I, Aquino D, et al. In vivo DTI tractography of the rat brain: an atlas of the main tracts in Paxinos space with histological comparison. *Magn. Reson. Imaging* 2015;33:296–303.
95. Johnson GA, Laoprasert R, Anderson RJ, et al. A multicontrast MR atlas of the Wistar rat brain. *Neuroimage* 2021;242:118470.
96. Wu Y-C, Field AS, Duncan ID, et al. High b-value and diffusion tensor imaging in a canine model of dysmyelination and brain maturation. *Neuroimage* 2011;58:829–837.
97. Bech J, Orłowski D, Glud AN, Dyrby TB, Sørensen JCH, Bjarkam CR. Ex vivo diffusion-weighted MRI tractography of the Göttingen minipig limbic system. *Brain Struct. Funct.* 2020;225:1055–1071.
98. Calabrese E, Badea A, Coe CL, et al. A diffusion tensor MRI atlas of the postmortem rhesus macaque brain. *Neuroimage* 2015;117:408–416.
99. Risser L, Sadoun A, Mescam M, et al. In vivo localization of cortical areas using a 3D computerized atlas of the marmoset brain. *Brain Struct. Funct.* 2019;224:1957–1969.
100. Feng L, Jeon T, Yu Q, et al. Population-averaged macaque brain atlas with high-resolution ex vivo DTI integrated into in vivo space. *Brain Struct. Funct.* 2017;222:4131–4147.
101. Liu C, Ye FQ, Newman JD, et al. A resource for the detailed 3D mapping of white matter pathways in the marmoset brain. *Nat. Neurosci.* 2020;23:271–280.
102. Sarubbo S, Petit L, De Benedictis A, Chioffi F, Ptito M, Dyrby TB. Uncovering the inferior fronto-occipital fascicle and its topological organization in non-human primates: the missing connection for language evolution. *Brain Struct. Funct.* 2019;224:1553–1567.
103. Rilling JK, Glasser MF, Preuss TM, et al. The evolution of the arcuate fasciculus revealed with comparative DTI. *Nat. Neurosci.* 2008;11:426–428.
104. Bryant KL, Li L, Eichert N, Mars RB. A comprehensive atlas of white matter tracts in the chimpanzee. *PLoS Biol.* 2020;18:e3000971.
105. Eichner C, Paquette M, Mildner T, et al. Increased sensitivity and signal-to-noise ratio in diffusion-weighted MRI using multi-echo acquisitions. *Neuroimage* 2020;221:117172.
106. Eichner C, Paquette M, Gallardo G, et al. High-resolution post-mortem diffusion MRI acquisitions for connectivity analyses in chimpanzees. In: 29th Annual Meeting of the International Society for Magnetic Resonance in Medicine (ISMRM). ; 2021. p. 1712.
107. Galinsky R, van de Looij Y, Mitchell N, et al. Magnetic Resonance Imaging Correlates of White Matter Gliosis and Injury in Preterm Fetal Sheep Exposed to Progressive Systemic Inflammation. *Int. J. Mol. Sci.* 2020;21 doi: 10.3390/ijms21238891.
108. Quezada S, van de Looij Y, Hale N, et al. Genetic and microstructural differences in the cortical plate of gyri and sulci during gyrification in fetal sheep. *Cereb. Cortex* 2020;30:6169–

6190.

109. Qiu A, Mori S, Miller MI. Diffusion tensor imaging for understanding brain development in early life. *Annu. Rev. Psychol.* 2015;66:853–876.
110. Jeurissen B, Tournier J-D, Dhollander T, Connelly A, Sijbers J. Multi-tissue constrained spherical deconvolution for improved analysis of multi-shell diffusion MRI data. *Neuroimage* 2014;103:411–426.
111. Miller JA, Ding S-L, Sunkin SM, et al. Transcriptional landscape of the prenatal human brain. *Nature* 2014;508:199–206.
112. Jiang X, Xu J, Gore JC. Mapping hepatocyte size in vivo using temporal diffusion spectroscopy MRI. *Magn. Reson. Med.* 2020;84:2671–2683.
113. Grussu F, Bernatowicz K, Casanova-Salas I, et al. Diffusion MRI signal cumulants and hepatocyte microstructure at fixed diffusion time: Insights from simulations, 9.4T imaging, and histology. *Magn. Reson. Med.* 2022 doi: 10.1002/mrm.29174.
114. Hill DK, Kim E, Teruel JR, et al. Diffusion-weighted MRI for early detection and characterization of prostate cancer in the transgenic adenocarcinoma of the mouse prostate model. *J. Magn. Reson. Imaging* 2016;43:1207–1217.
115. Panagiotaki E, Walker-Samuel S, Siow B, et al. Noninvasive quantification of solid tumor microstructure using VERDICT MRI. *Cancer Res.* 2014;74:1902–1912.
116. Grier MD, Zimmermann J, Heilbronner SR. Estimating Brain Connectivity With Diffusion-Weighted Magnetic Resonance Imaging: Promise and Peril. *Biol Psychiatry Cogn Neurosci Neuroimaging* 2020;5:846–854.
117. Schmahmann JD, Pandya D. *Fiber Pathways of the Brain*. OUP USA; 2009.
118. Swindler DR, Wood CD. *An Atlas of Primate Gross Anatomy: Baboon, Chimpanzee, and Man.*; 1973.
119. Hartig R, Glen D, Jung B, et al. The Subcortical Atlas of the Rhesus Macaque (SARM) for neuroimaging. *Neuroimage* 2021;235:117996.
120. Saleem KS, Logothetis NK. *A Combined MRI and Histology Atlas of the Rhesus Monkey Brain in Stereotaxic Coordinates*. Academic Press; 2012.
121. United States. National Institutes of Health. Public Health Services. *Stereotaxic Atlas of the Squirrel Monkey's Brain (Saimiri Sciureus).*; 1962.
122. Mandonnet E, Sarubbo S, Petit L. The Nomenclature of Human White Matter Association Pathways: Proposal for a Systematic Taxonomic Anatomical Classification. *Front. Neuroanat.* 2018;12:94.
123. Panesar SS, Fernandez-Miranda J. Commentary: The Nomenclature of Human White Matter Association Pathways: Proposal for a Systematic Taxonomic Anatomical Classification. *Front. Neuroanat.* 2019;13:61.
124. Schilling KG, Rheault F, Petit L, et al. Tractography dissection variability: What happens when 42 groups dissect 14 white matter bundles on the same dataset? *Neuroimage* 2021;243:118502.
125. Azadbakht H, Parkes LM, Haroon HA, et al. Validation of High-Resolution Tractography Against In Vivo Tracing in the Macaque Visual Cortex. *Cereb. Cortex* 2015;25:4299–4309.
126. van den Heuvel MP, de Reus MA, Feldman Barrett L, et al. Comparison of diffusion tractography and tract-tracing measures of connectivity strength in rhesus macaque connectome. *Hum. Brain Mapp.* 2015;36:3064–3075.
127. Shen K, Goulas A, Grayson DS, et al. Exploring the limits of network topology estimation

- using diffusion-based tractography and tracer studies in the macaque cortex. *NeuroImage* 2019;191:81–92 doi: 10.1016/j.neuroimage.2019.02.018.
128. Tang-Wright K, Smith JET, Bridge H, et al. Intra-Areal Visual Topography in Primate Brains Mapped with Probabilistic Tractography of Diffusion-Weighted Imaging. *Cereb. Cortex* 2022;32:2555–2574.
129. Schilling KG, Petit L, Rheault F, et al. Brain connections derived from diffusion MRI tractography can be highly anatomically accurate-if we know where white matter pathways start, where they end, and where they do not go. *Brain Struct. Funct.* 2020;225:2387–2402.
130. Gutierrez CE, Skibbe H, Nakae K, et al. Optimization and validation of diffusion MRI-based fiber tracking with neural tracer data as a reference. *Sci. Rep.* 2020;10:21285.
131. Girard G, Caminiti R, Battaglia-Mayer A, et al. On the cortical connectivity in the macaque brain: A comparison of diffusion tractography and histological tracing data. *Neuroimage* 2020;221:117201.
132. Thomas C, Ye FQ, Irfanoglu MO, et al. Anatomical accuracy of brain connections derived from diffusion MRI tractography is inherently limited. *Proc. Natl. Acad. Sci. U. S. A.* 2014;111:16574–16579.
133. Donahue CJ, Sotiropoulos SN, Jbabdi S, et al. Using Diffusion Tractography to Predict Cortical Connection Strength and Distance: A Quantitative Comparison with Tracers in the Monkey. *The Journal of Neuroscience* 2016;36:6758–6770 doi: 10.1523/jneurosci.0493-16.2016.
134. Schilling KG, Nath V, Hansen C, et al. Limits to anatomical accuracy of diffusion tractography using modern approaches. *Neuroimage* 2019;185:1–11.
135. Yan M, Yu W, Lv Q, et al. Mapping brain-wide excitatory projectome of primate prefrontal cortex at submicron resolution and comparison with diffusion tractography. *Elife* 2022;11 doi: 10.7554/eLife.72534.
136. Maffei C, Girard G, Schilling KG, et al. Insights from the IronTract challenge: Optimal methods for mapping brain pathways from multi-shell diffusion MRI. *Neuroimage* 2022;257:119327.
137. Grisot G, Haber SN, Yendiki A. Diffusion MRI and anatomic tracing in the same brain reveal common failure modes of tractography. *Neuroimage* 2021;239:118300.
138. Dyrby TB, Sogaard LV, Parker GJ, et al. Validation of in vitro probabilistic tractography. *Neuroimage* 2007;37:1267–1277.
139. Sauleau P, Lapouble E, Val-Laillet D, Malbert C-H. The pig model in brain imaging and neurosurgery. *Animal* 2009;3:1138–1151 doi: 10.1017/s1751731109004649.
140. Ryan MC, Sherman P, Rowland LM, et al. Miniature pig model of human adolescent brain white matter development. *J. Neurosci. Methods* 2018;296:99–108.
141. Wang R, Weng G, Yu S, Dai S, Zhang W, Zhu F. Diffusion-weighted imaging detects early brain injury after hypothermic circulatory arrest in pigs. *Interact. Cardiovasc. Thorac. Surg.* 2018;26:687–692.
142. Hutchinson EB, Schwerin SC, Radomski KL, Irfanoglu MO, Juliano SL, Pierpaoli CM. Quantitative MRI and DTI Abnormalities During the Acute Period Following CCI in the Ferret. *Shock* 2016;46:167–176.
143. Delettre C, Messé A, Dell L-A, et al. Comparison between diffusion MRI tractography and histological tract-tracing of cortico-cortical structural connectivity in the ferret brain. *Netw Neurosci* 2019;3:1038–1050.
144. Hamaide J, De Groof G, Van Steenkiste G, et al. Exploring sex differences in the adult zebra

- finch brain: In vivo diffusion tensor imaging and ex vivo super-resolution track density imaging. *Neuroimage* 2017;146:789–803.
145. Alexander DC, Dyrby TB, Nilsson M, Zhang H. Imaging brain microstructure with diffusion MRI: practicality and applications. *NMR Biomed.* 2019;32:e3841.
146. Novikov DS, Fieremans E, Jespersen SN, Kiselev VG. Quantifying brain microstructure with diffusion MRI: Theory and parameter estimation. *NMR Biomed.* 2019;32:e3998.
147. Jones DK. The effect of gradient sampling schemes on measures derived from diffusion tensor MRI: a Monte Carlo study. *Magn. Reson. Med.* 2004;51:807–815.
148. Zhang H, Schneider T, Wheeler-Kingshott CA, Alexander DC. NODDI: practical in vivo neurite orientation dispersion and density imaging of the human brain. *Neuroimage* 2012;61:1000–1016.
149. Lagore RL, Moeller S, Zimmermann J, et al. An 8-dipole transceive and 24-loop receive array for non-human primate head imaging at 10.5 T. *NMR Biomed.* 2021;34:e4472.
150. Gilbert KM, Gati JS, Klassen LM, et al. A geometrically adjustable receive array for imaging marmoset cohorts. *Neuroimage* 2017;156:78–86.
151. Gilbert KM, Schaeffer DJ, Gati JS, Klassen LM, Everling S, Menon RS. Open-source hardware designs for MRI of mice, rats, and marmosets: Integrated animal holders and radiofrequency coils. *J. Neurosci. Methods* 2019;312:65–72.
152. Slichter CP. *Principles of Magnetic Resonance.* Springer Science & Business Media; 2013.
153. Finch ED, Homer LD. Proton nuclear magnetic resonance relaxation measurements in frog muscle. *Biophys. J.* 1974;14:907–921.
154. Oros-Peusquens AM, Laurila M, Shah NJ. Magnetic field dependence of the distribution of NMR relaxation times in the living human brain. *MAGMA* 2008;21:131–147.
155. Chen N-K, Guidon A, Chang H-C, Song AW. A robust multi-shot scan strategy for high-resolution diffusion weighted MRI enabled by multiplexed sensitivity-encoding (MUSE). *Neuroimage* 2013;72:41–47.
156. Guhaniyogi S, Chu M-L, Chang H-C, Song AW, Chen N-K. Motion immune diffusion imaging using augmented MUSE for high-resolution multi-shot EPI. *Magn. Reson. Med.* 2016;75:639–652.
157. Mani M, Jacob M, Kelley D, Magnotta V. Multi-shot sensitivity-encoded diffusion data recovery using structured low-rank matrix completion (MUSSELS). *Magn. Reson. Med.* 2017;78:494–507.
158. Bertalan G, Boehm-Sturm P, Schreyer S, et al. The influence of body temperature on tissue stiffness, blood perfusion, and water diffusion in the mouse brain. *Acta Biomater.* 2019;96:412–420.
159. Abe Y, Tsurugizawa T, Le Bihan D. Water diffusion closely reveals neural activity status in rat brain loci affected by anesthesia. *PLoS Biol.* 2017;15:e2001494.
160. Yacoub E, Grier MD, Auerbach EJ, et al. Ultra-high field (10.5 T) resting state fMRI in the macaque. *Neuroimage* 2020;223:117349.
161. Autio JA, Zhu Q, Li X, et al. Minimal specifications for non-human primate MRI: Challenges in standardizing and harmonizing data collection. *Neuroimage* 2021;236:118082.
162. Gakuba C, Gaberel T, Goursaud S, et al. General Anesthesia Inhibits the Activity of the “Glymphatic System.” *Theranostics* 2018;8:710–722.
163. Zakszewski E, Schmit B, Kurpad S, Budde MD. Diffusion imaging in the rat cervical spinal cord. *J. Vis. Exp.* 2015 doi: 10.3791/52390.

164. Lindhardt TB, Gutiérrez-Jiménez E, Liang Z, Hansen B. Male and Female C57BL/6 Mice Respond Differently to Awake Magnetic Resonance Imaging Habituation. *Frontiers in Neuroscience* 2022;16 doi: 10.3389/fnins.2022.853527.
165. Stejskal EO, Tanner JE. Spin Diffusion Measurements: Spin Echoes in the Presence of a Time-Dependent Field Gradient. *J. Chem. Phys.* 1965;42:288–292.
166. Merboldt KD, Hänicke W, Frahm J. Diffusion imaging using stimulated echoes. *Magn. Reson. Med.* 1991;19:233–239.
167. Lundell H, Alexander DC, Dyrby TB. High angular resolution diffusion imaging with stimulated echoes: compensation and correction in experiment design and analysis. *NMR Biomed.* 2014;27:918–925.
168. Gore JC, Xu J, Colvin DC, Yankeelov TE, Parsons EC, Does MD. Characterization of tissue structure at varying length scales using temporal diffusion spectroscopy. *NMR Biomed.* 2010;23:745–756.
169. Cory DG, Garroway AN. Measurement of translational displacement probabilities by NMR: an indicator of compartmentation. *Magn. Reson. Med.* 1990;14:435–444.
170. Callaghan PT. *Translational Dynamics and Magnetic Resonance: Principles of Pulsed Gradient Spin Echo NMR.* OUP Oxford; 2011.
171. Ramanna S, Moss HG, McKinnon ET. Triple diffusion encoding MRI predicts intra-axonal and extra-axonal diffusion tensors in white matter. *Magnetic resonance* 2020.
172. Topgaard D. Multidimensional diffusion MRI. *J. Magn. Reson.* 2017;275:98–113.
173. Cheng, Cory. Multiple scattering by NMR. *J. Am. Chem. Soc.*
174. Özarlan E. Compartment shape anisotropy (CSA) revealed by double pulsed field gradient MR. *J. Magn. Reson.* 2009;199:56–67.
175. Paulsen JL, Özarlan E, Komlosh ME, Basser PJ, Song Y-Q. Detecting compartmental non-Gaussian diffusion with symmetrized double-PFG MRI. *NMR Biomed.* 2015;28:1550–1556.
176. Nilsson M, van Westen D, Ståhlberg F, Sundgren PC, Lätt J. The role of tissue microstructure and water exchange in biophysical modelling of diffusion in white matter. *MAGMA* 2013;26:345–370.
177. Ning L, Nilsson M, Lasič S, Westin C-F, Rathi Y. Cumulant expansions for measuring water exchange using diffusion MRI. *J. Chem. Phys.* 2018;148:074109.
178. Åslund I, Topgaard D. Determination of the self-diffusion coefficient of intracellular water using PGSE NMR with variable gradient pulse length. *J. Magn. Reson.* 2009;201:250–254.
179. Westin C-F, Knutsson H, Pasternak O, et al. Q-space trajectory imaging for multidimensional diffusion MRI of the human brain. *Neuroimage* 2016;135:345–362.
180. Lu Y, Yang Y, Connelly KA, Wright GA, Radau PE. Automated quantification of myocardial infarction using graph cuts on contrast delayed enhanced magnetic resonance images. *Quant. Imaging Med. Surg.* 2012;2:81–86.
181. Jelescu IO, Ciobanu L, Geffroy F, Marquet P, Le Bihan D. Effects of hypotonic stress and ouabain on the apparent diffusion coefficient of water at cellular and tissue levels in Aplysia. *NMR Biomed.* 2014;27:280–290.
182. McNab JA, Miller KL. Steady-state diffusion-weighted imaging: theory, acquisition and analysis. *NMR Biomed.* 2010;23:781–793.
183. Daniel BL, Granlund KL, Moran CJ, et al. Breast MRI without gadolinium: utility of 3D DESS, a new 3D diffusion weighted gradient-echo sequence. *Eur. J. Radiol.* 2012;81 Suppl 1:S24–6.

184. Sener RN. Echo-planar and gradient-echo diffusion MRI of normal brain iron in the globus pallidus. *Clin. Imaging* 2002;26:371–374.
185. Tyszka JM, Frank LR. High-field diffusion MR histology: image-based correction of eddy-current ghosts in diffusion-weighted rapid acquisition with relaxation enhancement (DW-RARE). *Magn. Reson. Med.* 2009;61:728–733.
186. Duyn JH, Yang Y, Frank JA, van der Veen JW. Simple Correction Method for Space Trajectory Deviations in MRI. *Journal of Magnetic Resonance* 1998;132:150–153 doi: 10.1006/jmre.1998.1396.
187. Alexander DC. A general framework for experiment design in diffusion MRI and its application in measuring direct tissue-microstructure features. *Magn. Reson. Med.* 2008;60:439–448.
188. Jones DK, Horsfield MA, Simmons A. Optimal strategies for measuring diffusion in anisotropic systems by magnetic resonance imaging. *Magnetic Resonance in Medicine* 1999;42:515–525 doi: 10.1002/(sici)1522-2594(199909)42:3<515::aid-mrm14>3.0.co;2-q.
189. Jensen JH, Helpert JA, Ramani A, Lu H, Kaczynski K. Diffusional kurtosis imaging: the quantification of non-gaussian water diffusion by means of magnetic resonance imaging. *Magn. Reson. Med.* 2005;53:1432–1440.
190. Kiselev VG, Il'yasov KA. Is the “biexponential diffusion” biexponential? *Magn. Reson. Med.* 2007;57:464–469.
191. Poot DHJ, den Dekker AJ, Achten E, Verhoye M, Sijbers J. Optimal experimental design for diffusion kurtosis imaging. *IEEE Trans. Med. Imaging* 2010;29:819–829.
192. Jillings S, Morez J, Vidas-Guscic N, et al. Multi-tissue constrained spherical deconvolution in a murine brain. In: *Proc Intl Soc Mag Reson Med* 28. ; 2020. p. 900.
193. Veraart J, Poot DHJ, Van Hecke W, et al. More accurate estimation of diffusion tensor parameters using diffusion Kurtosis imaging. *Magn. Reson. Med.* 2011;65:138–145.
194. Chuhutin A, Hansen B, Jespersen SN. Precision and accuracy of diffusion kurtosis estimation and the influence of b-value selection. *NMR in Biomedicine* 2017;30:e3777 doi: 10.1002/nbm.3777.
195. Hansen B, Jespersen SN. Data for evaluation of fast kurtosis strategies, b-value optimization and exploration of diffusion MRI contrast. *Sci Data* 2016;3:160072.
196. Hansen B, Lund TE, Sangill R, Jespersen SN. Experimentally and computationally fast method for estimation of a mean kurtosis. *Magn. Reson. Med.* 2013;69:1754–1760.
197. Hansen B, Lund TE, Sangill R, Stubbe E, Finsterbusch J, Jespersen SN. Experimental considerations for fast kurtosis imaging. *Magn. Reson. Med.* 2016;76:1455–1468.
198. Hansen B, Khan AR, Shemesh N, et al. White matter biomarkers from fast protocols using axially symmetric diffusion kurtosis imaging. *NMR Biomed.* 2017;30 doi: 10.1002/nbm.3741.
199. Hansen B, Jespersen SN. Recent Developments in Fast Kurtosis Imaging. *Frontiers in Physics* 2017;5 doi: 10.3389/fphy.2017.00040.
200. Ambrosen KS, Eskildsen SF, Hinne M, et al. Validation of structural brain connectivity networks: The impact of scanning parameters. *Neuroimage* 2020;204:116207.
201. Schilling KG, Tax CMW, Rheault F, et al. Fiber tractography bundle segmentation depends on scanner effects, vendor effects, acquisition resolution, diffusion sampling scheme, diffusion sensitization, and bundle segmentation workflow. *Neuroimage* 2021;242:118451.
202. Neher PF, Descoteaux M, Houde J-C, Stieltjes B, Maier-Hein KH. Strengths and weaknesses of state of the art fiber tractography pipelines--A comprehensive in-vivo and phantom

- evaluation study using Tractometer. *Med. Image Anal.* 2015;26:287–305.
203. Côté M-A, Girard G, Boré A, Garyfallidis E, Houde J-C, Descoteaux M. Tractometer: towards validation of tractography pipelines. *Med. Image Anal.* 2013;17:844–857.
204. Shen K, Bezgin G, Schirner M, Ritter P, Everling S, McIntosh AR. A macaque connectome for large-scale network simulations in TheVirtualBrain. *Sci Data* 2019;6:123.
205. Daducci A, Canales-Rodríguez EJ, Descoteaux M, et al. Quantitative comparison of reconstruction methods for intra-voxel fiber recovery from diffusion MRI. *IEEE Trans. Med. Imaging* 2014;33:384–399.
206. Girard G, Daducci A, Petit L, et al. AxTract: Toward microstructure informed tractography. *Hum. Brain Mapp.* 2017;38:5485–5500.
207. Daducci A, Dal Palú A, Descoteaux M, Thiran J-P. Microstructure Informed Tractography: Pitfalls and Open Challenges. *Front. Neurosci.* 2016;10:247.
208. Daducci A, Dal Palú A, Lemkaddem A, Thiran J-P. COMMIT: Convex optimization modeling for microstructure informed tractography. *IEEE Trans. Med. Imaging* 2015;34:246–257.
209. Smith RE, Tournier J-D, Calamante F, Connelly A. SIFT: Spherical-deconvolution informed filtering of tractograms. *Neuroimage* 2013;67:298–312.
210. Smith RE, Tournier J-D, Calamante F, Connelly A. SIFT2: Enabling dense quantitative assessment of brain white matter connectivity using streamlines tractography. *Neuroimage* 2015;119:338–351.
211. Pestilli F, Yeatman JD, Rokem A, Kay KN, Wandell BA. Evaluation and statistical inference for human connectomes. *Nat. Methods* 2014;11:1058–1063.
212. Palombo M, Ianus A, Guerreri M, et al. SANDI: A compartment-based model for non-invasive apparent soma and neurite imaging by diffusion MRI. *Neuroimage* 2020;215:116835.
213. Zhang J, Lemberskiy G, Moy L, Fieremans E, Novikov DS, Kim SG. Measurement of cellular-interstitial water exchange time in tumors based on diffusion-time-dependent diffusional kurtosis imaging. *NMR Biomed.* 2021;34:e4496.
214. Jelescu IO, de Skowronski A, Palombo M, Novikov DS. Neurite Exchange Imaging (NEXI): A minimal model of diffusion in gray matter with inter-compartment water exchange. *arXiv [physics.med-ph]* 2021.
215. Olesen JL, Østergaard L, Shemesh N, Jespersen SN. Diffusion time dependence, power-law scaling, and exchange in gray matter. *arXiv [physics.med-ph]* 2021.
216. Hill I, Palombo M, Santin M, et al. Machine learning based white matter models with permeability: An experimental study in cuprizone treated in-vivo mouse model of axonal demyelination. *Neuroimage* 2021;224:117425.
217. Lasič S, Lundell H, Topgaard D, Dyrby TB. Effects of imaging gradients in sequences with varying longitudinal storage time-Case of diffusion exchange imaging. *Magn. Reson. Med.* 2018;79:2228–2235.
218. Vos SB, Tax CMW, Luijten PR, Ourselin S, Leemans A, Froeling M. The importance of correcting for signal drift in diffusion MRI. *Magn. Reson. Med.* 2017;77:285–299.
219. Malyarenko D, Galbán CJ, Londy FJ, et al. Multi-system repeatability and reproducibility of apparent diffusion coefficient measurement using an ice-water phantom. *J. Magn. Reson. Imaging* 2013;37:1238–1246.
220. Fieremans E, Lee H-H. Physical and numerical phantoms for the validation of brain microstructural MRI: A cookbook. *Neuroimage* 2018;182:39–61.
221. Liao C, Bilgic B, Tian Q, et al. Distortion-free, high-isotropic-resolution diffusion MRI with

- gSlider BUDA-EPI and multicoil dynamic B shimming. *Magn. Reson. Med.* 2021;86:791–803.
222. Setsompop K, Fan Q, Stockmann J, et al. High-resolution in vivo diffusion imaging of the human brain with generalized slice dithered enhanced resolution: Simultaneous multislice (gSlider-SMS). *Magn. Reson. Med.* 2018;79:141–151.
223. Tian Q, Li Z, Fan Q, et al. SDnDTI: Self-supervised deep learning-based denoising for diffusion tensor MRI. *NeuroImage* 2022;253:119033 doi: 10.1016/j.neuroimage.2022.119033.
224. Ning L, Setsompop K, Rathi Y. A combined compressed sensing super-resolution diffusion and gSlider-SMS acquisition/reconstruction for rapid sub-millimeter whole-brain diffusion imaging.; 2016.
225. Holdsworth SJ, O'Halloran R, Setsompop K. The quest for high spatial resolution diffusion-weighted imaging of the human brain in vivo. *NMR Biomed.* 2019;32:e4056.
226. Boretius S, Natt O, Watanabe T, et al. In vivo diffusion tensor mapping of the brain of squirrel monkey, rat, and mouse using single-shot STEAM MRI. *MAGMA* 2004;17:339–347.
227. Zhang J, Zhang X. Diffusion-Weighted Imaging of the Macaque Brain Using Diffusion-Prepared Turbo Spin Echo in MRI. *Applied Sciences* 2021;11:12077 doi: 10.3390/app112412077.
228. Ortiz-Rios M, Balezeau F, Haag M, Schmid MC, Kaiser M. Dynamic reconfiguration of macaque brain networks during natural vision. *Neuroimage* 2021;244:118615.
229. Lamy J, Romain L, Ouhmich F. Dicomifier.; 2021. doi: 10.5281/zenodo.4459178.
230. Jeurissen B, Leemans A, Sijbers J. Automated correction of improperly rotated diffusion gradient orientations in diffusion weighted MRI. *Med. Image Anal.* 2014;18:953–962.
231. Schilling KG, Yeh F-C, Nath V, et al. A fiber coherence index for quality control of B-table orientation in diffusion MRI scans. *Magn. Reson. Imaging* 2019;58:82–89.
232. Veraart J, Novikov DS, Christiaens D, Ades-Aron B, Sijbers J, Fieremans E. Denoising of diffusion MRI using random matrix theory. *Neuroimage* 2016;142:394–406.
233. Kellner E, Dhital B, Kiselev VG, Reisert M. Gibbs-ringing artifact removal based on local subvoxel-shifts. *Magn. Reson. Med.* 2016;76:1574–1581.
234. Lee H-H, Novikov DS, Fieremans E. Removal of partial Fourier-induced Gibbs (RPG) ringing artifacts in MRI. *Magn. Reson. Med.* 2021;86:2733–2750.
235. Bautista T, O'Muircheartaigh J, Hajnal JV, Tournier J-D. Removal of Gibbs ringing artefacts for 3D acquisitions using subvoxel shifts. In: *Proceedings of the International Society for Magnetic Resonance in Medicine.* ; 2021.
236. Andersson JLR, Sotiropoulos SN. An integrated approach to correction for off-resonance effects and subject movement in diffusion MR imaging. *Neuroimage* 2016;125:1063–1078.
237. Hansen CB, Nath V, Hainline AE, et al. Characterization and correlation of signal drift in diffusion weighted MRI. *Magn. Reson. Imaging* 2019;57:133–142.
238. Ades-Aron B, Veraart J, Kochunov P, et al. Evaluation of the accuracy and precision of the diffusion parameter ESTimation with Gibbs and Noise removal pipeline. *Neuroimage* 2018;183:532–543.
239. Cai LY, Yang Q, Hansen CB, et al. PreQual: An automated pipeline for integrated preprocessing and quality assurance of diffusion weighted MRI images. *Magn. Reson. Med.* 2021;86:456–470.
240. Tournier J-D, Smith R, Raffelt D, et al. MRtrix3: A fast, flexible and open software framework for medical image processing and visualisation. *Neuroimage* 2019;202:116137.
241. Lohmeier J, Kaneko T, Hamm B, Makowski MR, Okano H. atlasBRESX: Automated template-

- derived brain extraction in animal MRI. *Sci. Rep.* 2019;9:12219.
242. Wang H, Yushkevich PA. Multi-atlas segmentation with joint label fusion and corrective learning—an open source implementation. *Frontiers in Neuroinformatics* 2013;7 doi: 10.3389/fninf.2013.00027.
243. Chakravarty MM, Steadman P, van Eede MC, et al. Performing label-fusion-based segmentation using multiple automatically generated templates. *Hum. Brain Mapp.* 2013;34:2635–2654.
244. Wang X, Li X-H, Cho JW, et al. U-net model for brain extraction: Trained on humans for transfer to non-human primates. *Neuroimage* 2021;235:118001.
245. Hsu L-M, Wang S, Walton L, Wang T-WW, Lee S-H, Shih Y-YI. 3D U-Net Improves Automatic Brain Extraction for Isotropic Rat Brain Magnetic Resonance Imaging Data. *Front. Neurosci.* 2021;15:801008.
246. Coupeau P, Fasquel J-B, Mazerand E, Menei P, Montero-Menei CN, Dinomais M. Patch-based 3D U-Net and transfer learning for longitudinal piglet brain segmentation on MRI. *Comput. Methods Programs Biomed.* 2022;214:106563.
247. Manjón JV, Coupé P, Concha L, Buades A, Louis Collins D, Robles M. Diffusion Weighted Image Denoising Using Overcomplete Local PCA. *PLoS ONE* 2013;8:e73021 doi: 10.1371/journal.pone.0073021.
248. Muckley MJ, Ades-Aron B, Papaioannou A, et al. Training a neural network for Gibbs and noise removal in diffusion MRI. *Magn. Reson. Med.* 2021;85:413–428.
249. Veraart J, Fieremans E, Jelescu IO, Knoll F, Novikov DS. Gibbs ringing in diffusion MRI. *Magn. Reson. Med.* 2016;76:301–314.
250. Perrone D, Aelterman J, Pižurica A, Jeurissen B, Philips W, Leemans A. The effect of Gibbs ringing artifacts on measures derived from diffusion MRI. *Neuroimage* 2015;120:441–455.
251. Koay CG, Basser PJ. Analytically exact correction scheme for signal extraction from noisy magnitude MR signals. *J. Magn. Reson.* 2006;179:317–322.
252. İanuş A, Carvalho J, Fernandes FF, et al. Soma and Neurite Density MRI (SANDI) of the in-vivo mouse brain and comparison with the Allen Brain Atlas. *Neuroimage* 2022;254:119135.
253. Horsfield MA, Sala S, Neema M, et al. Rapid semi-automatic segmentation of the spinal cord from magnetic resonance images: application in multiple sclerosis. *Neuroimage* 2010;50:446–455.
254. De Leener B, Kadoury S, Cohen-Adad J. Robust, accurate and fast automatic segmentation of the spinal cord. *Neuroimage* 2014;98:528–536.
255. Gros C, De Leener B, Badji A, et al. Automatic segmentation of the spinal cord and intramedullary multiple sclerosis lesions with convolutional neural networks. *Neuroimage* 2019;184:901–915.
256. De Leener B, Lévy S, Dupont SM, et al. SCT: Spinal Cord Toolbox, an open-source software for processing spinal cord MRI data. *Neuroimage* 2017;145:24–43.
257. De Leener B, Taso M, Cohen-Adad J, Callot V. Segmentation of the human spinal cord. *MAGMA* 2016;29:125–153.
258. De Leener B, Mangeat G, Dupont S, et al. Topologically preserving straightening of spinal cord MRI. *J. Magn. Reson. Imaging* 2017 doi: 10.1002/jmri.25622.
259. De Leener B, Fonov VS, Collins DL, Callot V, Stikov N, Cohen-Adad J. PAM50: Unbiased multimodal template of the brainstem and spinal cord aligned with the ICBM152 space. *Neuroimage* 2018;165:170–179.

260. Gros C, Asiri A, De Leener B, et al. Ex vivo MRI template of the human cervical cord at 80 $\mu$ m isotropic resolution. In: Proceedings of the 28th Annual Meeting of ISMRM, Sydney, Australia. ; 2020.
261. Saliani A, Zaimi A, Nami H, Duval T, Stikov N, Cohen-Adad J. Construction of a rat spinal cord atlas of axon morphometry. *Neuroimage* 2019;202:116156.
262. Cohen-Adad J, Alonso-Ortiz E, Abramovic M, et al. Open-access quantitative MRI data of the spinal cord and reproducibility across participants, sites and manufacturers. *Sci Data* 2021;8:219.
263. Nery F, Szczepankiewicz F, Kerkelä L, et al. In vivo demonstration of microscopic anisotropy in the human kidney using multidimensional diffusion MRI. *Magn. Reson. Med.* 2019;82:2160–2168.
264. Kjølby BF, Khan AR, Chuhutin A, et al. Fast diffusion kurtosis imaging of fibrotic mouse kidneys. *NMR Biomed.* 2016;29:1709–1719.
265. Panagiotaki E, Chan RW, Dikaios N, et al. Microstructural Characterization of Normal and Malignant Human Prostate Tissue With Vascular, Extracellular, and Restricted Diffusion for Cytometry in Tumours Magnetic Resonance Imaging. *Invest. Radiol.* 2015;50:218.
266. Chatterjee A, Bourne RM, Wang S, et al. Diagnosis of Prostate Cancer with Noninvasive Estimation of Prostate Tissue Composition by Using Hybrid Multidimensional MR Imaging: A Feasibility Study. *Radiology* 2018;287:864–873.
267. Lemberskiy G, Fieremans E, Veraart J, Deng F-M, Rosenkrantz AB, Novikov DS. Characterization of prostate microstructure using water diffusion and NMR relaxation. *Front. Phys.* 2018;6 doi: 10.3389/fphy.2018.00091.
268. Zhang J, Zhang G, Morrison B, Mori S, Sheikh KA. Magnetic resonance imaging of mouse skeletal muscle to measure denervation atrophy. *Exp. Neurol.* 2008;212:448–457.
269. Welsh CL, DiBella EVR, Hsu EW. Higher-Order Motion-Compensation for In Vivo Cardiac Diffusion Tensor Imaging in Rats. *IEEE Trans. Med. Imaging* 2015;34:1843–1853.
270. Perez-Lopez R, Mateo J, Mossop H, et al. Diffusion-weighted Imaging as a Treatment Response Biomarker for Evaluating Bone Metastases in Prostate Cancer: A Pilot Study. *Radiology* 2017;283:168–177.
271. Bailey C, Collins DJ, Tunariu N, et al. Microstructure Characterization of Bone Metastases from Prostate Cancer with Diffusion MRI: Preliminary Findings. *Front. Oncol.* 2018;8:26.
272. Zhou Z, Xu M-J, Gao B. Hepatocytes: a key cell type for innate immunity. *Cell. Mol. Immunol.* 2016;13:301–315.
273. Behrens TEJ, Woolrich MW, Jenkinson M, et al. Characterization and propagation of uncertainty in diffusion-weighted MR imaging. *Magn. Reson. Med.* 2003;50:1077–1088.
274. Cui Y, Dyvorne H, Besa C, Cooper N, Taouli B. IVIM diffusion-weighted imaging of the liver at 3.0T: Comparison with 1.5T. *Eur. J. Radiol. Open* 2015;2:123–128.
275. Immonen R, Smith G, Brady RD, et al. Harmonization of pipeline for preclinical multicenter MRI biomarker discovery in a rat model of post-traumatic epileptogenesis. *Epilepsy Res.* 2019;150:46–57.
276. Neher P, Stieltjes B, Wolf I, Meinzer H-P, Maier-Hein K. Analysis of tractography biases introduced by anisotropic voxels.; 2013.
277. Meola A, Comert A, Yeh F-C, Stefanescu L, Fernandez-Miranda JC. The controversial existence of the human superior fronto-occipital fasciculus: Connectome-based tractographic study with microdissection validation. *Hum. Brain Mapp.* 2015;36:4964–4971.

278. Thiebaut de Schotten M, Dell'Acqua F, Valabregue R, Catani M. Monkey to human comparative anatomy of the frontal lobe association tracts. *Cortex* 2012;48:82–96.
279. Yeatman JD, Weiner KS, Pestilli F, Rokem A, Mezer A, Wandell BA. The vertical occipital fasciculus: a century of controversy resolved by in vivo measurements. *Proc. Natl. Acad. Sci. U. S. A.* 2014;111:E5214–23.
280. Warrington S, Bryant KL, Khrapitchev AA, et al. XTRACT - Standardised protocols for automated tractography in the human and macaque brain. *Neuroimage* 2020;217:116923.
281. Schilling KG, Gao Y, Stepniewska I, et al. The VALiDATe29 MRI Based Multi-Channel Atlas of the Squirrel Monkey Brain. *Neuroinformatics* 2017;15:321–331.
282. Doderio L, Vascon S, Murino V, Bifone A, Gozzi A, Sona D. Automated multi-subject fiber clustering of mouse brain using dominant sets. *Front. Neuroinform.* 2014;8:87.
283. Wasserthal J, Neher P, Maier-Hein KH. TractSeg - Fast and accurate white matter tract segmentation. *Neuroimage* 2018;183:239–253.
284. Wakana S, Caprihan A, Panzenboeck MM, et al. Reproducibility of quantitative tractography methods applied to cerebral white matter. *Neuroimage* 2007;36:630–644.
285. Yeatman JD, Dougherty RF, Myall NJ, Wandell BA, Feldman HM. Tract profiles of white matter properties: automating fiber-tract quantification. *PLoS One* 2012;7:e49790.
286. Smith SM, Jenkinson M, Johansen-Berg H, et al. Tract-based spatial statistics: voxelwise analysis of multi-subject diffusion data. *Neuroimage* 2006;31:1487–1505.
287. Yeh F-C. Shape analysis of the human association pathways. *Neuroimage* 2020;223:117329.
288. Treuting PM, Dintzis SM, Montine KS. *Comparative Anatomy and Histology: A Mouse, Rat, and Human Atlas.* Academic Press; 2017.
289. Paxinos G, Halliday G, Watson C, Kassem MS. *Atlas of the Developing Mouse Brain.* Academic Press; 2020.
290. McLaren DG, Kosmatka KJ, Oakes TR, et al. A population-average MRI-based atlas collection of the rhesus macaque. *Neuroimage* 2009;45:52–59.
291. Van Essen DC, Glasser MF, Dierker DL, Harwell J. Cortical parcellations of the macaque monkey analyzed on surface-based atlases. *Cereb. Cortex* 2012;22:2227–2240.
292. Vos SB, Viergever MA, Leemans A. The anisotropic bias of fractional anisotropy in anisotropically acquired DTI data.; 2011.
293. Alexander DC, Barker GJ. Optimal imaging parameters for fiber-orientation estimation in diffusion MRI. *Neuroimage* 2005;27:357–367.
294. Jones R, Grisot G, Augustinack J, et al. Insight into the fundamental trade-offs of diffusion MRI from polarization-sensitive optical coherence tomography in ex vivo human brain. *Neuroimage* 2020;214:116704.
295. Schilling K, Gao Y, Janve V, Stepniewska I, Landman BA, Anderson AW. Can increased spatial resolution solve the crossing fiber problem for diffusion MRI? *NMR Biomed.* 2017;30 doi: 10.1002/nbm.3787.
296. Maier-Hein KH, Neher PF, Houde J-C, et al. The challenge of mapping the human connectome based on diffusion tractography. *Nat. Commun.* 2017;8:1349.
297. Schilling KG, Tax CMW, Rheault F, et al. Prevalence of white matter pathways coming into a single white matter voxel orientation: The bottleneck issue in tractography. *Hum. Brain Mapp.* 2021 doi: 10.1002/hbm.25697.

298. Reveley C, Seth AK, Pierpaoli C, et al. Superficial white matter fiber systems impede detection of long-range cortical connections in diffusion MR tractography. *Proc. Natl. Acad. Sci. U. S. A.* 2015;112:E2820–8.
299. Aydogan DB, Jacobs R, Dulawa S, et al. When tractography meets tracer injections: a systematic study of trends and variation sources of diffusion-based connectivity. *Brain Struct. Funct.* 2018;223:2841–2858.
300. Wilkinson MD, Dumontier M, Aalbersberg IJJ, et al. The FAIR Guiding Principles for scientific data management and stewardship. *Sci Data* 2016;3:160018.
301. Gorgolewski KJ, Auer T, Calhoun VD, et al. The brain imaging data structure, a format for organizing and describing outputs of neuroimaging experiments. *Sci Data* 2016;3:160044.
302. Martone M, Goscinski W, Das S, et al. Call for community review of the Brain Imaging Data Structure – a standard for organizing and describing MRI data sets. *F1000Res.* 2018;7:1368.
303. Gholam J, Szczepankiewicz F, Tax CMW, et al. aDWI-BIDS: an extension to the brain imaging data structure for advanced diffusion weighted imaging. *arXiv [physics.med-ph]* 2021.
304. Bourget M-H, Kametsky L, Ghosh SS, et al. Microscopy-BIDS: An Extension to the Brain Imaging Data Structure for Microscopy Data. *Frontiers in Neuroscience* 2022;16 doi: 10.3389/fnins.2022.871228.